Chemical Product and Process Modeling

Volume 4, *Issue* 1 2009 *Article* 17

Suspension Mixing Tank - Design Heuristic

Jimmy Lea*

*The University of New South Wales, j.lea@unswalumni.com

Copyright ©2009 The Berkeley Electronic Press. All rights reserved.

Suspension Mixing Tank - Design Heuristic*

Jimmy Lea

Abstract

The design of suspension mixing tanks is often embedded in empiricism due to insufficient understanding of the hydrodynamics of dense solid-liquid interaction. This is particularly limiting during the design of mixing tanks or batch reactor for expensive high quality products in the fine chemicals, biological and pharmaceutical processing industries. In this paper, a computational fluid dynamics (CFD)-assisted design approach has been employed to study the effectiveness of mixing tank geometrical configurations to suspend particles. Ten crucial variables were investigated and the effects of changing the value of these variables were documented. In addition, a multivariable study involving these ten variables was also conducted to investigate the most important variables among them. Finally, by capturing the essence of the results, a design heuristic was developed which can be applied across the process industry.

KEYWORDS: computational fluid dynamics, CFD, chemical engineering, bombs, explosives manufacturing, applied mathematics, modelling and simulation, mixing tank, batch reactor, suspensions, particles

---

*The author is grateful to Mr. Paul Flavel, Operations Manager of Australian Defence Industries (ADI) – Mulwala high explosives manufacturing facility, for sponsoring this process R&D project. The author is equally grateful to Dr. Patrick O'Flaherty of ADI – Garden Island naval base, for his supports and encouragement of this research project.

1. INTRODUCTION

In the process industry, suspension of particles denser than its fluid media is one of the most common and important goal to be achieved. Achieving complete suspension of the particles leads to homogeneous suspension whilst achieving partial success leads to inhomogeneity and eventually product quality issues. Despite the industrial relevance of this operation, especially in high explosive manufacturing facilities, the impact on the performance of the suspension mixing tank through changing several crucial variables had received little research attention. Whilst several recent researches were conducted in this field [Laakkonen et al. 2007; Alliet-Gaubert et al. 2006; Aubin and Xuereb 2006; Lewis and Ochieng 2006], none conducted a comprehensive study that specifically addressed all the crucial variables. Moreover, in many instances, the design of a mixing tank for suspending particles was largely based on empirical data. Consequently, operators had to work with sub-optimum process conditions which inevitably led to poor product quality, consistency and yield. The study aims are to fill this research gap and to use the available information for designing an effective suspension mixing tank or the optimisation of an existing tank.

Significant improvements in the design capability and reliability of suspension mixing tank may be expected from advances in computational fluid dynamics (CFD) simulation technology. CFD offers a cost-effective means of capturing the hydrodynamic phenomena and the ability to quantify the performance of a suspension mixing tank [Sommerfeld and Decker 2004]. The results of this study are applicable across the broad spectrum of the manufacturing study. For example, not only can the results of this study be applied to the manufacture of high explosives and bombs, it can also be applied across a broad range of industries such as but not limited to the chemical, bioprocess, pharmaceutical, petrochemical and mineral processing industries.

Despite the broad applicability of these results, they are only applicable to popular cylindrical suspension mixing tank and do not apply to square mixing tanks [Kresta et al. 2006 and Kilander et al. 2007]. Moreover, the results are only applicable to dished bottom tanks which was selected as the preferred tank bottom since the just suspended speed, N_{js} is a function of tank bottom and that a flat bottom requires 10-20% higher N_{js} to suspend solid particles. It is also known that for solid suspension in flat-bottomed tank, the solids tend to accumulate in the corners whilst conical bottom must be avoided due to their ineffectiveness to assist in suspending solids [Paul et al. 2004].

2. STUDY AIMS

The aims of this present paper are to:

1. Provide a design approach based on the fundamental equations governing the hydrodynamics of multiphase solid-liquid system.
2. Propose mathematical models as a function of the changes made to each variable under investigation
3. Propose a design heuristic based on the newly discovered information
4. Fill research gap in this field and to provide engineers a platform to start their design of an effective system or to optimise an existing system

3. METHODOLOGY

3.1 Variables investigated

Ten crucial variables that have profound effect on the ability of a mixing tank to suspend particles were investigated, namely: [1] shaft to impeller diameter (d/D), [2] blade width to impeller diameter (W/D), [3] impeller to tank diameter (D/T), [4] number of blades (N_B), [5] impeller clearance to tank diameter ratio (C/T), [6] impeller rotational speed (N), [7] baffle width to tank diameter ratio (B/T) and [8] baffle off-wall spacing to tank diameter ratio (b/T), [9] number of baffles (N_{BF}) and [10] number of impellers (N_I).

Overall, these ten variables constitute the crucial parameters that govern the success of a given geometrical configuration in suspending particles. The impeller employed was a standard 6-bladed 45^o pitch blade turbine. The quantitative performance of each trial condition was captured via surface integration of the plane where the flow passed through. Then integrated values were plotted as a function of each variable.

3.2 Key performance indicator

To perform an impartial quantitative analysis, a horizontal plane across the impeller was created so that surface integration can be performed to determine the axial flow passing through the impeller (Figure 1). Because of such arrangement, computation excluded the radial flow component. The amount of axial flow passing through this plane is the key performance indicator (KPI) and is used as the basis of quantitative comparison of the performance of one variable to another.

DOI: 10.2202/1934-2659.1334

Figure 1: Key performance indicator

The one-factor-at-a-time trial conditions for all ten variables mentioned in Section 3.1 are shown in Table 1.

4. THEORETICAL CONSIDERATIONS

4.1 Simulation theory

Fluent 6.3 solver was used to create a numerical solution that matches the governing conservation equations. The Navier-Stokes equation, shown in Equation (1) provides the usual starting point for the analysis of flow processes. The finite volume (FV) method uses the integral form of the conservation of equations as its starting point to ensure global conservation. The differential

Table 1: One-factor-at-a-time trial conditions and results

Trials	*d/D*	*W/D*	*D/T*	N_B	*C/T*	*N*	*B/T*	*b/T*	N_{BF}	N_I	$\dot{m}$	*P*
1	0.080	0.23	0.5	6	0.76	80	0.071	0.0187	4	1	**1,251**	**5,858**
2	0.094	0.23	0.5	6	0.76	80	0.071	0.0187	4	1	**1,245**	**5,800**
3	0.131	0.23	0.5	6	0.76	80	0.071	0.0187	4	1	**1,238**	**5,741**
4	0.169	0.23	0.5	6	0.76	80	0.071	0.0187	4	1	**1,229**	**5,683**
5	0.200	0.23	0.5	6	0.76	80	0.071	0.0187	4	1	**1,225**	**5,624**
6	0.08	0.1	0.5	6	0.76	80	0.071	0.0187	4	1	**943**	**3,398**
7	0.08	0.3	0.5	6	0.76	80	0.071	0.0187	4	1	**1,328**	**6,796**
8	0.08	0.4	0.5	6	0.76	80	0.071	0.0187	4	1	**1,401**	**8,143**
9	0.08	0.5	0.5	6	0.76	80	0.071	0.0187	4	1	**1,455**	**9,608**
10	0.08	0.7	0.5	6	0.76	80	0.071	0.0187	4	1	**1,496**	**12,712**
11	0.08	0.25 m	0.15	6	0.76	80	0.071	0.0187	4	1	**4.042**	**26.50**
12	0.08	0.25 m	0.30	6	0.76	80	0.071	0.0187	4	1	**488**	**586**
13	0.08	0.25 m	0.35	6	0.76	80	0.071	0.0187	4	1	**651**	**1,172**
14	0.08	0.25 m	0.40	6	0.76	80	0.071	0.0187	4	1	**866**	**2,109**
15	0.08	0.25 m	0.55	6	0.76	80	0.071	0.0187	4	1	**1,255**	**9,432**
16	0.08	0.25 m	0.60	6	0.76	80	0.071	0.0187	4	1	**1,150**	**14,821**
17	0.08	0.25 m	0.70	6	0.76	80	0.071	0.0187	4	1	**861**	**28,845**
18	0.08	0.23	0.5	0	0.76	80	0.071	0.0187	4	1	**0**	**202**
19	0.08	0.23	0.5	2	0.76	80	0.071	0.0187	4	1	**991**	**2,519**
20	0.08	0.23	0.5	3	0.76	80	0.071	0.0187	4	1	**1,105**	**3,398**
21	0.08	0.23	0.5	4	0.76	80	0.071	0.0187	4	1	**1,160**	**4,394**
22	0.08	0.23	0.5	8	0.76	80	0.071	0.0187	4	1	**1,257**	**6,913**
23	0.08	0.23	0.5	6	0.15	80	0.071	0.0187	4	1	**1,170**	**7,206**
24	0.08	0.23	0.5	6	0.20	80	0.071	0.0187	4	1	**1,215**	**6342**
25	0.08	0.23	0.5	6	0.30	80	0.071	0.0187	4	1	**1,272**	**5,331**
26	0.08	0.23	0.5	6	0.4	80	0.071	0.0187	4	1	**1,284**	**5,335**
27	0.08	0.23	0.5	6	0.50	80	0.071	0.0187	4	1	**1,280**	**5,565**
28	0.08	0.23	0.5	6	0.60	80	0.071	0.0187	4	1	**1,271**	**5,858**
29	0.08	0.23	0.5	6	0.68	80	0.071	0.0187	4	1	**1,260**	**5,855**
30	0.08	0.23	0.5	6	0.76	20	0.071	0.0187	4	1	**312**	**88**
31	0.08	0.23	0.5	6	0.76	100	0.071	0.0187	4	1	**1,565**	**11,424**
32	0.08	0.23	0.5	6	0.76	120	0.071	0.0187	4	1	**1,878**	**19,772**
33	0.08	0.23	0.5	6	0.76	140	0.071	0.0187	4	1	**2,191**	**31,474**
34	0.08	0.23	0.5	6	0.76	80	0.063	0.0187	4	1	**1,215**	**5,725**
35	0.08	0.23	0.5	6	0.76	80	0.083	0.0187	4	1	**1,273**	**6,173**
36	0.08	0.23	0.5	6	0.76	80	0.100	0.0187	4	1	**1,298**	**6,371**
37	0.08	0.23	0.5	6	0.76	80	0.110	0.0187	4	1	**1,300**	**6,420**
38	0.08	0.23	0.5	6	0.76	80	0.115	0.0187	4	1	**1,292**	**6,390**
39	0.08	0.23	0.5	6	0.76	80	0.125	0.0187	4	1	**1,266**	**6,348**
40	0.08	0.23	0.5	6	0.76	80	0.071	0.0167	4	1	**1,249**	**5,858**
41	0.08	0.23	0.5	6	0.76	80	0.071	0.0250	4	1	**1,252**	**5,893**
42	0.08	0.23	0.5	6	0.76	80	0.071	0.0350	4	1	**1256**	**5,917**
43	0.08	0.23	0.5	6	0.76	80	0.071	0.0500	4	1	**1,247**	**5,917**
44	0.08	0.23	0.5	6	0.76	80	0.071	0.0750	4	1	**1,211**	**5,800**
45	0.08	0.23	0.5	6	0.76	80	0.071	0.0900	4	1	**1,197**	**5,741**
46	0.08	0.23	0.5	6	0.76	80	0.071	0.1000	4	1	**1,193**	**5,683**
47	0.08	0.23	0.5	6	0.76	80	0.071	0.0187	0	1	**903**	**5,003**
48	0.08	0.23	0.5	6	0.76	80	0.071	0.0187	2	1	**1,094**	**5,414**
49	0.08	0.23	0.5	6	0.76	80	0.071	0.0187	3	1	**1,189**	**5,598**
50	0.08	0.23	0.5	6	0.76	80	0.071	0.0187	5	1	**1,290**	**6,110**
51	0.08	0.23	0.5	6	0.76	80	0.071	0.0187	6	1	**1,313**	**6,261**
52	0.08	0.23	0.5	6	0.76	80	0.071	0.0187	12	1	**1,399**	**7,342**
53	0.08	0.23	0.5	6	0.76	80	0.071	0.0187	20	1	**1,438**	**7,543**
54	0.08	0.23	0.5	6	0.76	80	0.071	0.0187	4	0	**0**	**200**
55	0.08	0.23	0.5	6	0.76	80	0.071	0.0187	4	2	**1,295**	**5,858**
56	0.08	0.23	0.5	6	0.76	80	0.071	0.0187	4	3	**1,323**	**8,498**
57	0.08	0.23	0.5	6	0.76	80	0.071	0.0187	4	4	**1,346**	**10,761**
58	0.08	0.23	0.5	6	0.76	80	0.071	0.0187	4	5	**1,360**	**12,303**

DOI: 10.2202/1934-2659.1334

equation is integrated over the volume of each cell to obtain algebraic equations. Variable values are stored at the cell centres and interpolation is used to express variable values at cell faces in terms of the cell centre values. Surface and volume integrals are estimated using appropriate quadrature formulae.

$$\rho \frac{D\upsilon}{Dt} = -\nabla p + \mu \nabla^2 \upsilon + \rho g \qquad - 1$$

In this study, the focus was on solving the conservation of mass, momentum and turbulence transport with a view to generating a steady-state 3D hydrodynamics profile.

4.2 Numerical setup

The numerical setups involved in this part of the study were similar to those employed and elaborated in Lea et al. [2005]. To simulate impeller rotations, separate rotational zones in the immediate vicinity of the impellers were created and a multiple reference frame (MRF) approach was employed. Fluent's default under-relaxation values were used in all simulation runs. In this simulation, the segregated-implicit approach was adopted. All simulations were started using the first-order upwind scheme and upon convergence of the results, were switched to second-order upwind scheme or QUICK scheme in the case of the volume fraction.

With baffled tank, due to the lack of solid body rotation, the Realizable k-ε model was employed to capture the turbulence phenomena. The term 'realisable' means that the model satisfies certain mathematical constraints on the normal stresses, consistent with the physics of turbulent flows. This model aims to overcome the weakness poses by the standard k-ε or other conventional k-ε models [Rahimi and Parvareh 2005]. The corresponding transport equations are given in Equations (2) and (3).

$$\frac{\partial}{\partial t}(\rho k) + \frac{\partial}{\partial x_j}(\rho k u_j) = -\frac{\partial}{\partial x_i}\left[(\mu + \frac{u_t}{\sigma_k})\frac{\partial k}{\partial x_j}\right] + G_k + G_b - \rho\varepsilon - Y_M + S_k \qquad - 2$$

$$\frac{\partial}{\partial t}(\rho \varepsilon) + \frac{\partial}{\partial x_j}(\rho \varepsilon u_j) = \frac{\partial}{\partial x_j}\left[(\mu + \frac{u_t}{\sigma_\varepsilon})\frac{\partial \varepsilon}{\partial x_j}\right] + \rho C_1 S_\varepsilon - \rho C_2 \frac{\varepsilon^2}{k + \sqrt{v\varepsilon}} + C_{1\varepsilon}\frac{\varepsilon}{k} C_{3\varepsilon} G_b + S_\varepsilon \qquad - 3$$

In the two equations above, G_k represents the turbulence kinetic energy generated due to the mean velocity gradients whereas G_b is the turbulence kinetic energy due to buoyancy. Y_M represents the contribution of the fluctuating dilation in compressible turbulence to the overall dissipation rate. C_2 and $C_{1\varepsilon}$ are constants whilst σ_k and σ_ε are the turbulent Prandtl numbers for k and ε respectively.

PRESTO (pressure staggering option) was employed to compute the pressure value at the cell surface by interpolating the value at cell centroid. SIMPLE algorithm was used for the pressure-velocity coupling. VOF model was used to simulate the hydrodynamics of air draw-down whilst the Mixture and Eulerian models were used to capture the hydrodynamics of RDX particles to be suspended and aluminium particles to be drawn down. Simulations were generally considered converged when the residuals for mass, momentum and turbulence kinetic energy and its dissipation rate fell below 1×10^{-4}. Further checks for convergence were made by creating a monitoring point inside the tank to ensure that the value monitored remained constant with further iterations. This further helps to ensure results integrity.

To model the multiphase phenomena associated with the suspension of RDX particles in the mixing tank, an appropriate model must be selected from the models available in Euler-Lagrange or the Euler-Euler approach. The three different models available in the Euler-Euler approach include the VOF model, the Mixture model and the Eulerian model. Whilst the VOF model is more suitable for simulating phenomena such as the draw-down of air or water into the primary phase, the Mixture and Eulerian models are suitable for simulating the suspension of particles in the primary phase. As a general guide, there are two parameters that assist in the identification of an appropriate multiphase model for those situations where the use of VOF model is inappropriate. The first parameter is the particulate loading and the second parameter is the Stokes number. The results showed that the Mixture model was the most appropriate.

4.3 Validation

A CFD model validation study was successfully performed via particles image velocimetry (PIV) experiment and the details can be obtained in Lea et al. [2005]. The same validated-model was employed for the simulations described in this paper. This ensures the reliability of the models used in this investigation and hence, the integrity of the results presented.

4.4 Grid independence test

To ensure convergence and obtain accurate results, the quality of the cells must be examined prior to starting the simulation. For mixing simulation such as this, the

DOI: 10.2202/1934-2659.1334

EquiAngle Skew should not exceed 0.85 for hexahedral and 0.9 for tetrahedral cells. In this study, no cell has an EquiAngle Skew value that breaches these criteria. Hence it was safe to assume that the overall cells had quality high enough to promote convergence and accuracy during computation.

A preliminary grid convergence study was performed to verify that the solution obtained from using the second-order upwind discretisation scheme was mesh independent. Grid independence tests were carried out on trials 1 and 14. For trial 1, the results show that at 447,495 cells, the mass flowrate was 1,251 kg s^{-1} whilst at 639,693 cells, the mass flowrate was 1,255 kg s^{-1}. In other words, an increase in 42.95% in the number of cells will change the mass flowrate value by 0.3197%. For trial 14, the results show that at 467,436 cells the mass flowrate was 1,255 kg s^{-1} and at 646,744 cells, the mass flowrate was 1,259 kg s^{-1}. This translates into a 0.3187% increase for an increase of 38.36% in the number of cells. These grid independence tests show that the economical number of cells suitable for this variable study is anything between 400,000 and 500,000, which will not compromise the results integrity.

Figure 2 shows a typical geometry meshed with tetrahedral cells. The number of cells inside and outside the rotational zones was systematically increased in the x-, y- and z-directions throughout the tank. When refining the mesh, care was taken to assign additional cells to the regions of high gradient around the impeller blades and discharge regions.

5. RESULTS AND DISCUSSION – SINGLE VARIABLE ANALYSIS

In this section, the results of each variable are presented in the following order:

1. A graph of mass flowrate through the plane created versus the variable under investigation
2. A mathematical model for the results is proposed to capture the behaviour of varying the variable
3. A graph of power consumed versus the variable under investigation
4. A mathematical model is proposed for power consumption analysis

In a few cases, vector plots are presented to provide a deeper insight into the hydrodynamics of the fluid movement.

In all the mathematical models proposed, the minimum regression is $\geq$ 0.97.

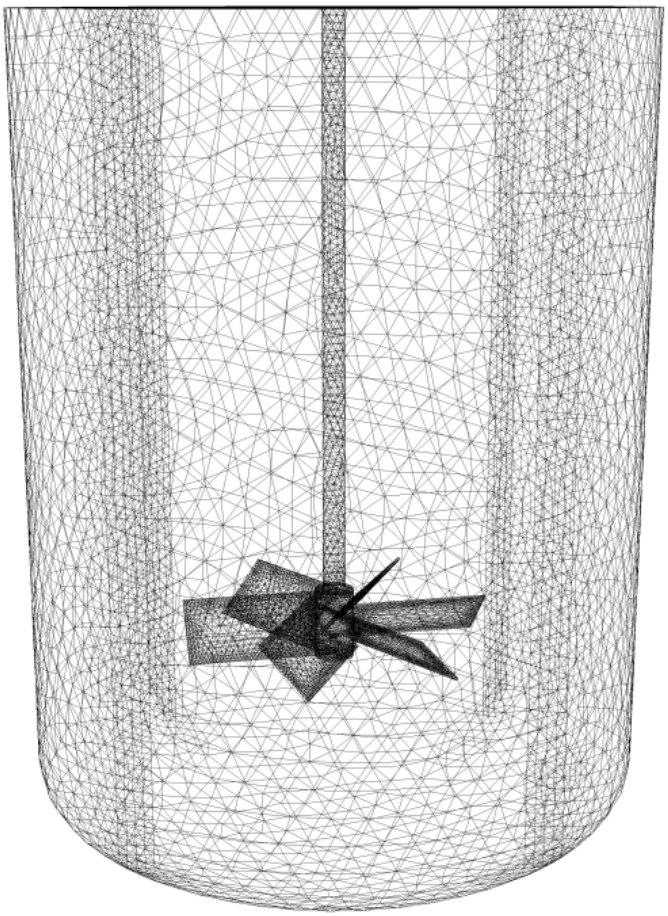

Figure 2: Geometry meshed with tetrahedral cells

5.1 Shaft diameter to impeller diameter ratio

Figure 3 shows a power relationship between the mass flowrate of flow passing through the plane and the shaft diameter to impeller diameter ratio. It is obvious that *d/D* is inversely proportional to the mass flowrate and follows a power function with a good regression of 0.9923, in the form:

$$\dot{m} = 1181\left(\frac{d}{D}\right)^{-0.0226} \qquad \text{- 4}$$

DOI: 10.2202/1934-2659.1334

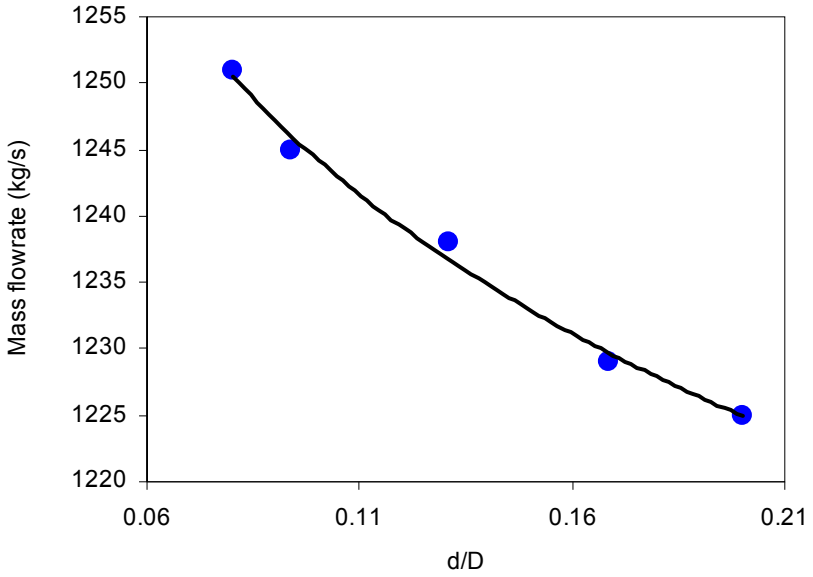

Figure 3: Mass flowrate vs d/D

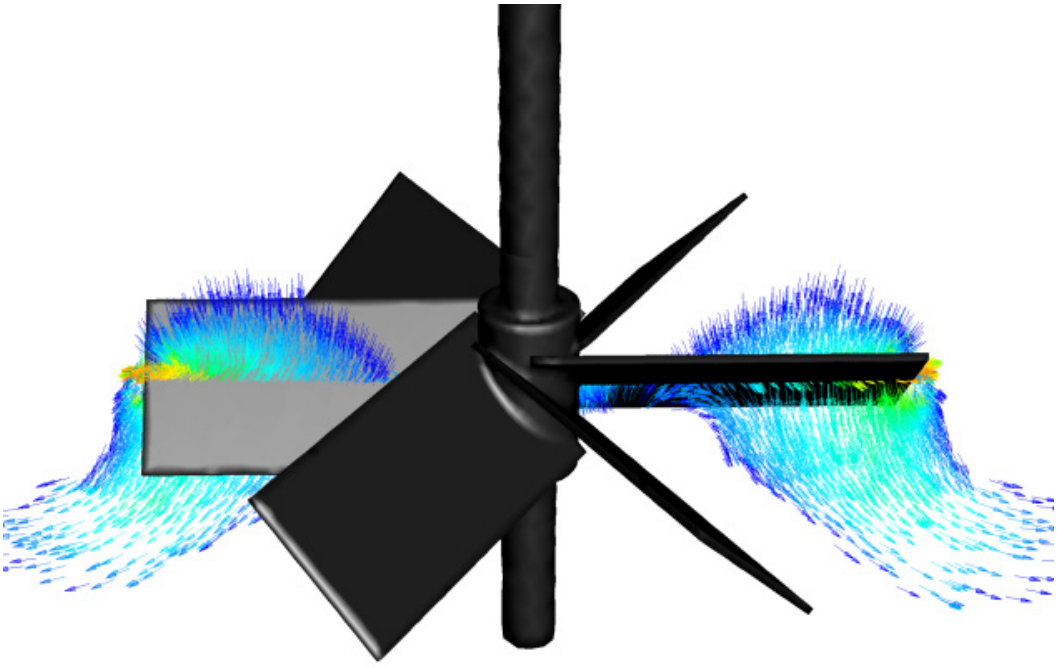

Figure 4: Vector plot of d/D = 0.08

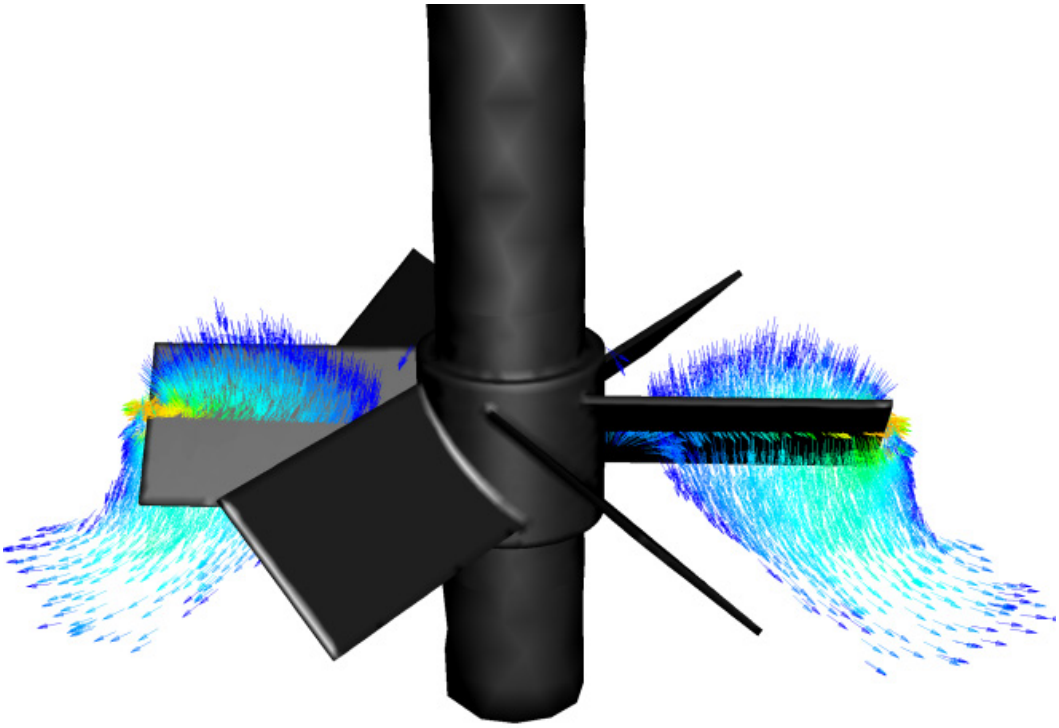

Figure 5: Vector plot of d/D = 0.2

Figures 4 and 5 show that although the shaft diameter has been increased by 150%, the flow profile remains the same. The slight reduction in the mass flowrate when the shaft diameter was increased gradually was attributed to the high flow discharge being located at the blade tip and low flow discharge in the vicinity of the shaft hub.

DOI: 10.2202/1934-2659.1334

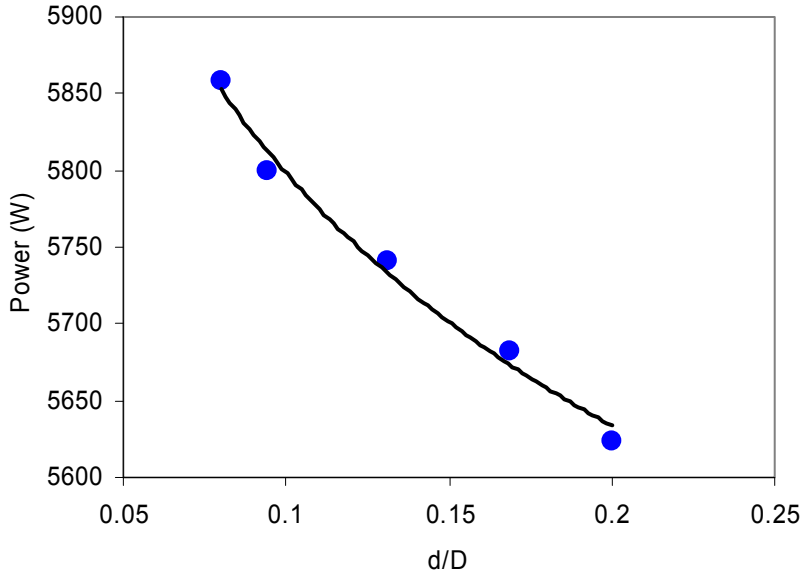

Figure 6: Power consumed in kilowatts vs d/D

The power consumption in kilowatts as a function of shaft diameter to impeller diameter ratio, as shown in Figure 6, follows a power relationship with good regression of 0.9867, in the form:

$$P = 5268\left(\frac{d}{D}\right)^{-0.0416} \qquad - 5$$

An increase in *d/D* from 0.08 to 0.2 reduced the power consumption by only 3.742%. That is, for every 1% increment in *d/D*, the power consumption will reduce by 2.5%. From a practical perspective, it is more beneficial to minimise the shaft diameter without compromising the minimum shaft diameter and maximise the blade length within a given impeller diameter.

5.2 Blade width to impeller diameter ratio

Figure 7 shows the relationship between the mass flowrate and the blade width to impeller diameter ratio.

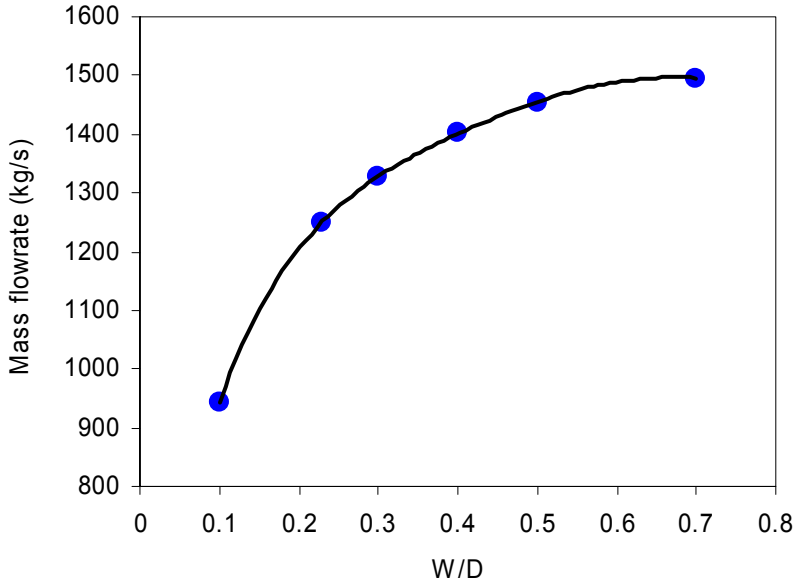

Figure 7: Mass flowrate vs W/D

The behaviour is described by the model:

$$\dot{m} = \frac{a\left(\frac{W}{D}\right)}{1 + b\left(\frac{W}{D}\right)} \qquad - 6$$

$\dot{m}$ represented mass flowrate and *W/D* represented the blade width to impeller diameter ratio. Data regression to Equation (6) yielded a=20,000 kg s^{-1} and b=12 with an excellent correlation fit of 1.

When *W/D* was increased by 200% from 0.1 - 0.3, the increase in flowrate was 43.44%, that is, a 1% increase in *W/D* increased the flowrate by 0.2172%. When *W/D* was increased by 25% from 0.4 - 0.5, the increase in flowrate was only 3.595%, that is, a 1% increase in *W/D* increased the flowrate by 0.1438%. Beyond this range, the percentage increase in the axial flowrate decreased as the graph levelled. A 400% increase in *W/D* from 0.5 - 0.7, resulted in an increase of 4.199%, that is, a 1% increase in *W/D* increased the flowrate by a 0.01050%.

DOI: 10.2202/1934-2659.1334

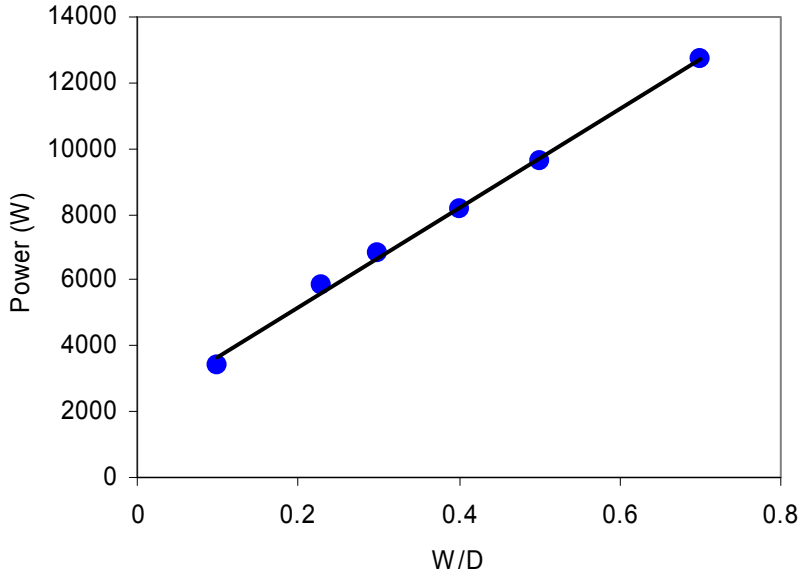

Figure 8: Power consumed in kilowatts vs W/D

The power consumption as a function of the blade width to impeller diameter ratio, as shown in Figure 8, has a linear relationship, with a good regression of 0.9972. The expression is given by:

$$P = 15162\left(\frac{W}{D}\right) + 2117 \qquad - 7$$

Equation (7) shows that a 1% increase in *W/D* will increase the power consumption by 0.5890%.Every time the blade width is increased, there will be an increase in the power consumption [Kumaresan and Joshi 2006]. However, beyond *W/D*=0.3, a higher blade width aspect ratio does not render economic feasibility, whilst below *W/D*=0.1, the flowrate generated may not be sufficient to suspend the particles. Therefore, the optimum performance is $0.1 \leq W/D \leq 0.3$.

5.3 Impeller diameter to tank diameter ratio

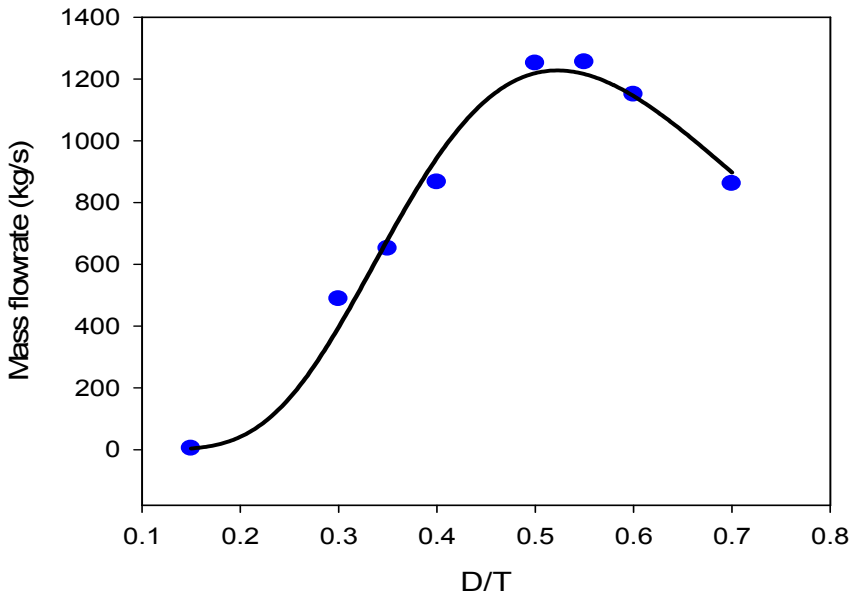

Figure 9: Mass flowrate vs *D/T*

Figure 9 shows the relationship between the mass flowrate and the impeller diameter to tank diameter ratio and is governed by the following expression, with a good regression value of 0.9901:

$$\dot{m} = ae^{\left[-0.5\left(\ln\left(\frac{(D/T)}{x_0}\right)/b\right)^2\right]} \qquad - 8$$

Conducting a non-linear regression on Equation (8), yielded a=1,228 kg s^{-1}, b=0.3693, x_0=0.5226 with excellent regression of R=0.9925.

The maximum value was located at D/T = 0.5226

DOI: 10.2202/1934-2659.1334

Increasing the *D/T* ratio from 0.15 - 0.55 increased the mass flowrate however, increasing the *D/T* value beyond the maximum value caused a reduction in the mass flowrate. Between *D/T* = 0.3 - 0.4 (33% increment), the increase in mass flowrate was 138.1%, between *D/T* = 0.4 - 0.55 (37.50% increment), the increase was 28.69% and between *D/T* = 0.55 - 0.6 (9.09% increment), the reduction in flowrate was 5.839%. Between *D/T* = 0.6 – 0.7 (16.67% increment), there was a sharp decrease in mass flowrate by 21.59%. Thus, for optimum performance: $0.5 \leq D/T \leq 0.55$. This result agrees with Tatterson [1994].

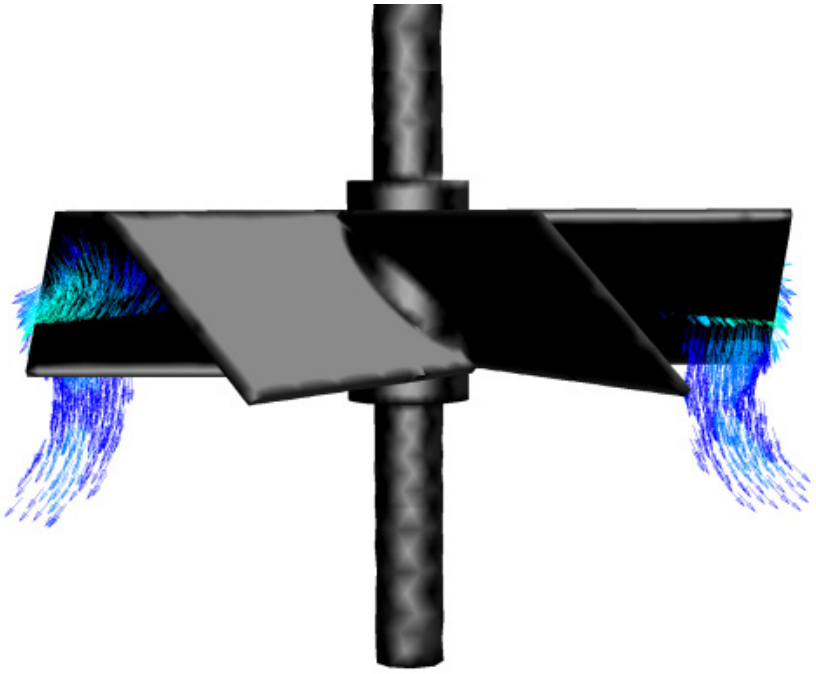

Figure 10: Vector plot of *D/T* = 0.4

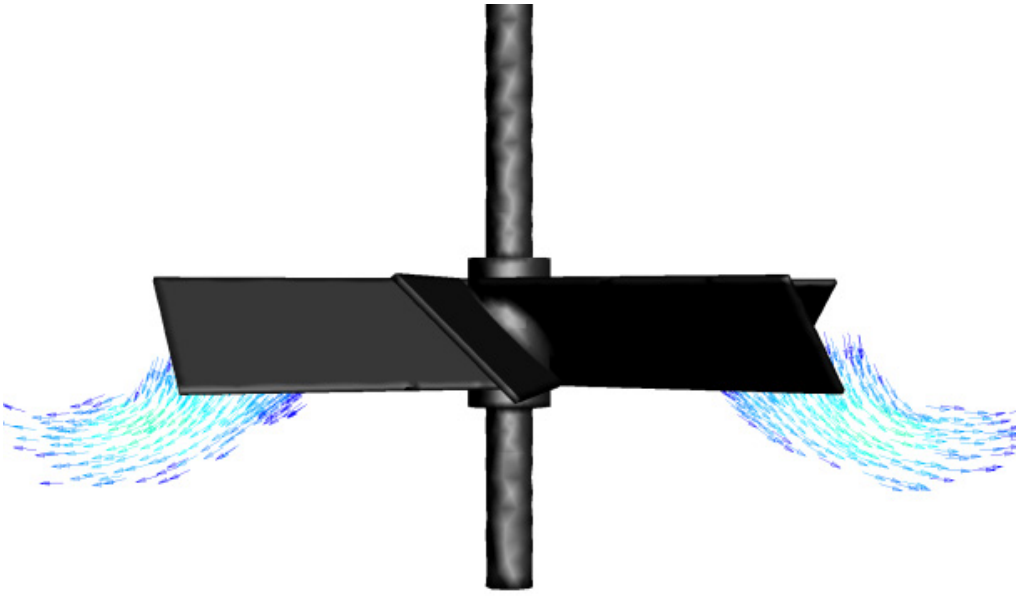

Figure 11: Vector plot of $D/T = 0.55$

The reduction in the mass flowrate when the D/T ratio was increased to value beyond the maximum value, was attributed to the change in the flow profile discharged by the impellers. Figure 10 shows that at $D/T = 0.4$, the flow discharge was axial in nature but when $D/T = 0.55$, the flow changed from axial flow to radial flow as shown by the vector plot in Figure 11. Obviously, because of this the amount of fluid that passed through the horizontal plane decreased per unit time.

Figure 12 shows the power consumed in kilowatts when D/T was increased from 0.15 to 0.7. The plot follows an exponential relationship with a good regression of 0.9971 in the form:

$$P = 130e^{7.74\left(\frac{D}{T}\right)} \qquad - 9$$

Between $D/T = 0.3 - 0.4$, the increase in power consumption was 116.9%, between $D/T = 0.4 - 0.55$, the increased power consumption was 219.3% and between $D/T = 0.55 - 0.6$, the increased in power consumption was 47.24%. Finally, from $D/T = 0.6 – 0.7$, the increase in power consumption was 116.8%. Thus, increasing D/T is always accompanied by the increase in power consumption [Kumaresan and Joshi 2006]. From the mass flowrate and power consumption analyses, it was observed that between $D/T = 0.4 - 0.55$, there was a huge power consumption increment because this was the effective range to deliver massive flow in the axial direction.

DOI: 10.2202/1934-2659.1334

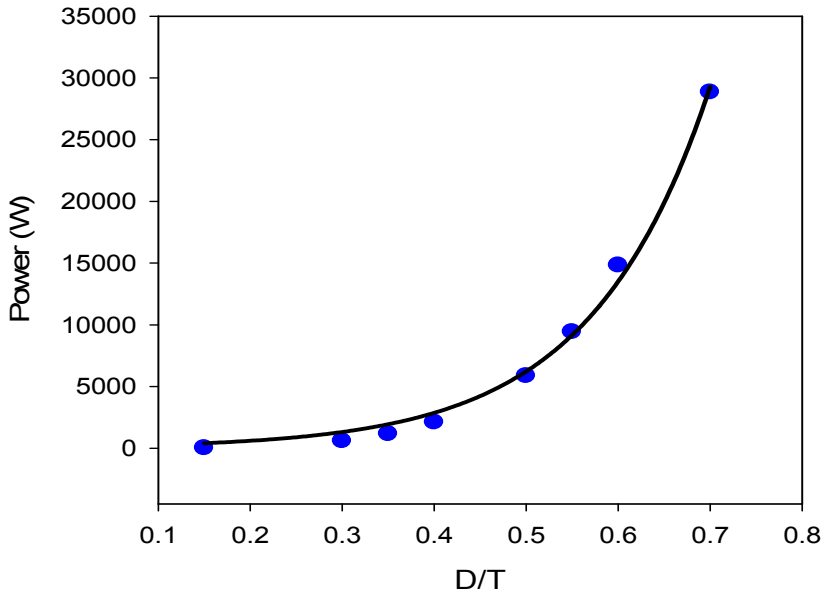

Figure 12: Power consumed in kilowatts vs *D/T*

5.4 Number of blades in the impeller

Figure 13 shows the relationship between the mass flowrate and the impeller diameter to tank diameter ratio and is governed by the following model:

$$\dot{m} = \frac{aN_B}{1 + bN_B} \qquad - 10$$

where $\dot{m}$ represents mass flowrate and N_B represents the number of blades. Data regression to Equation (10) yielded a=1,717 kg s^{-1} and b=1.226 with an excellent correlation fit of 0.9943. The increase in mass flowrate when the number of blades was increased from 2 to 3 blades was 10.65%, from 3 to 4 blades was 5.631%, from 4 to 6 was 6.019% and from 6 to 8 blades was 3.082% [Kumaresan and Joshi 2006]. Increasing the number of blades from 6 to 8 did not return a significantly higher mass flowrate value. The advantage of using a 6-bladed impeller is that it delivers more axial flow per unit time, attainable at a lower impeller rotational speed. In contrast, to produce the same amount of axial flow per unit time, the speed required from a 4-bladed impeller is higher. This is important for processes where a lower impeller rotational speed is needed, yet a high axial flow is desired to meet the process objective.

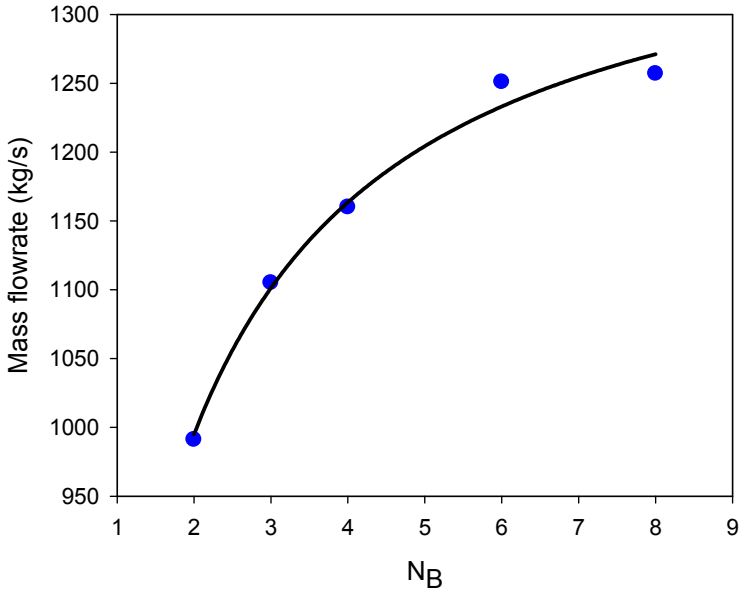

Figure 13: Mass flowrate vs number of blades

Despite such an advantage, the use of a 6-bladed impeller requires a thicker shaft, which means in some plants, may involve overhauling the entire mixing tank rather than simply swapping existing impeller with a 6-bladed impeller.

The power consumed as a function of the number of blades, shown in Figure 14, can be represented by the correlation with good regression of 0.9998, in the form:

$$P = P_0 + a\left(1 - e^{-b(N_B)}\right) \qquad - 11$$

P is the power consumed in W, whereas P_0=202 W and is the power consumed when there are no blades on the impeller, that is, no impeller on the shaft. A non-linear regression analysis on Equation (11) yielded a=11,134 W, b=0.1164. Increasing from 4 to 6 blades will increase the power consumption by 33.38% and 16.35% from 6 to 8 blades [Kumaresan and Joshi 2006]. In addition to the advantages and disadvantages of using 6-bladed impeller outlined above, the use of 6-bladed impeller will increase the power consumption as well. Therefore, the use of either 4 or 6-bladed impeller is dependent on the plant situation and can only be prescribed on a case-by-case basis.

DOI: 10.2202/1934-2659.1334

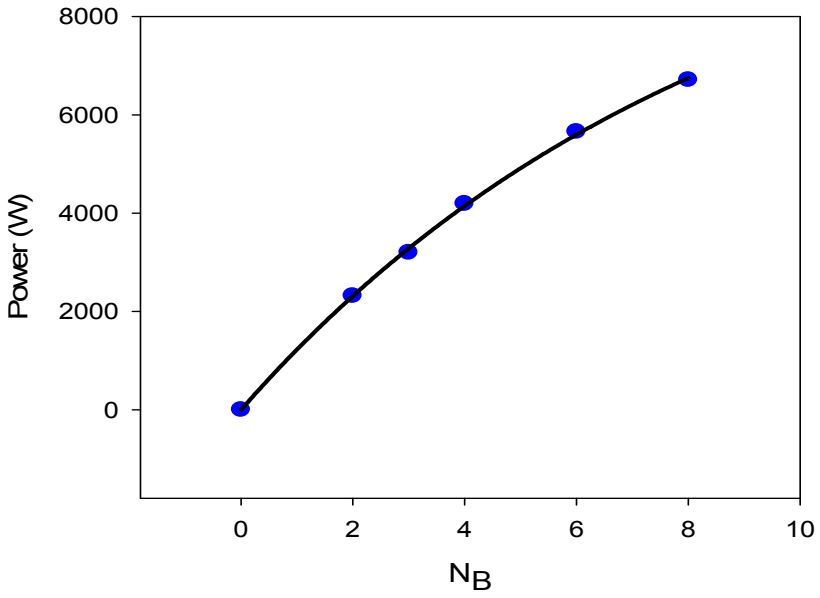

Figure 14: Power consumed in kilowatts vs number of blades

5.5 Impeller bottom clearance

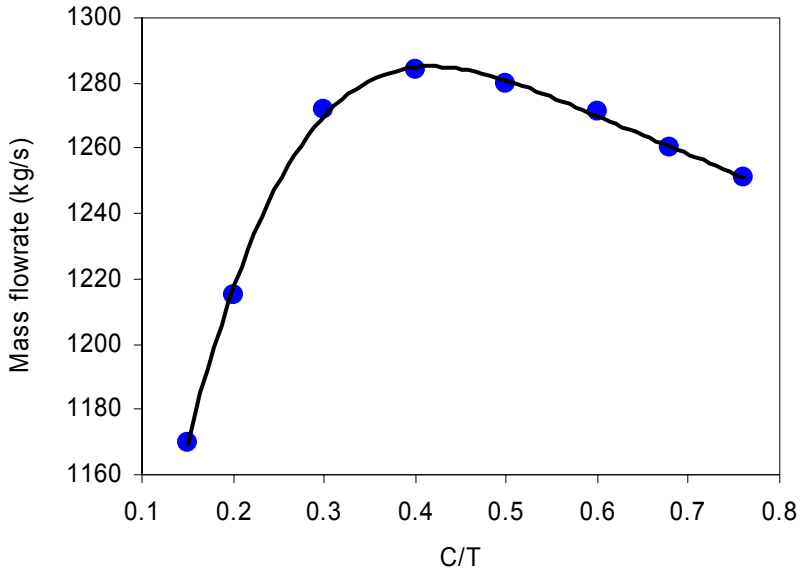

Figure 15: Mass flowrate vs C/T

Figure 15 shows the relationship between the mass flowrate and the impeller bottom clearance to tank diameter ratio and is governed by:

$$\dot{m} = \frac{a\left(\frac{C}{T}\right)}{\left[1+b\left(\frac{C}{T}\right)\right]^2} \qquad \text{- 12}$$

$\dot{m}$ represented mass flowrate and *C/T* represented the impeller bottom clearance to tank diameter ratio. Data regression to Equation (12) yielded a = 13,840 kg s^{-1} and b = 2.565 with a good correlation fit of 0.9943. For maximum values,

The maximum value was located at $\left(\frac{C}{T}\right) = 0.3898$

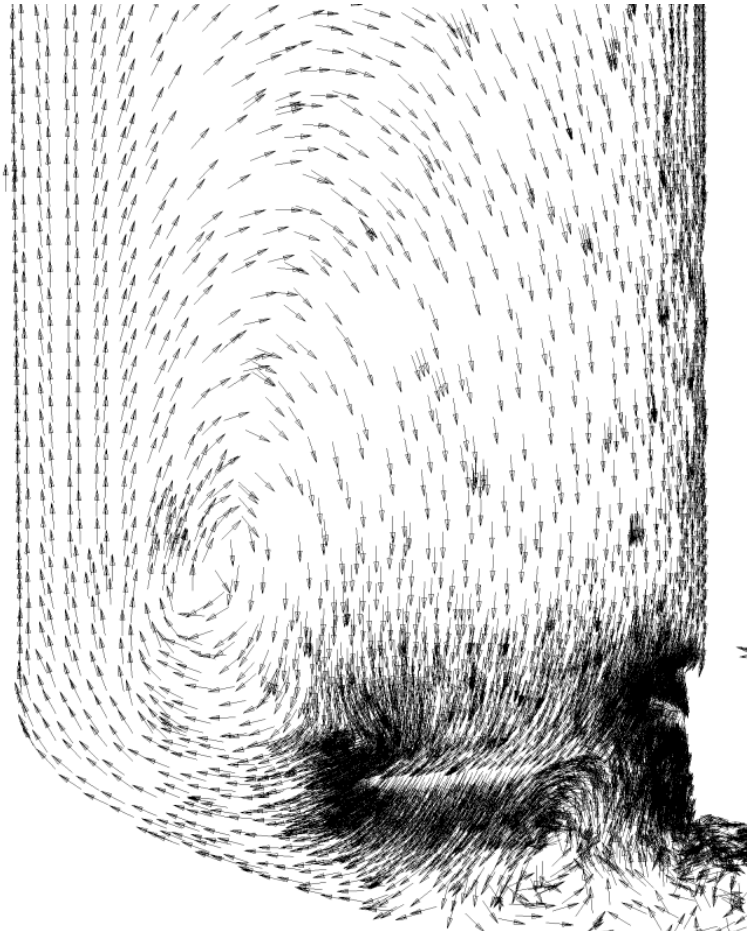

Figure 16: Vector plot at C/T=0.15

DOI: 10.2202/1934-2659.1334

When the impeller was located too close to the tank bottom, as shown in Figure 16, a lower axial flowrate was obtained because of the narrow clearance between the tank bottom and the impeller for the flow to naturally deflect according to the curvature of the tank bottom. The narrow clearance prevented the development of axial discharge from the impellers, forcing the flow discharge to traverse radially. As a result, a significant amount of radial flow was produced in place of axial flow.

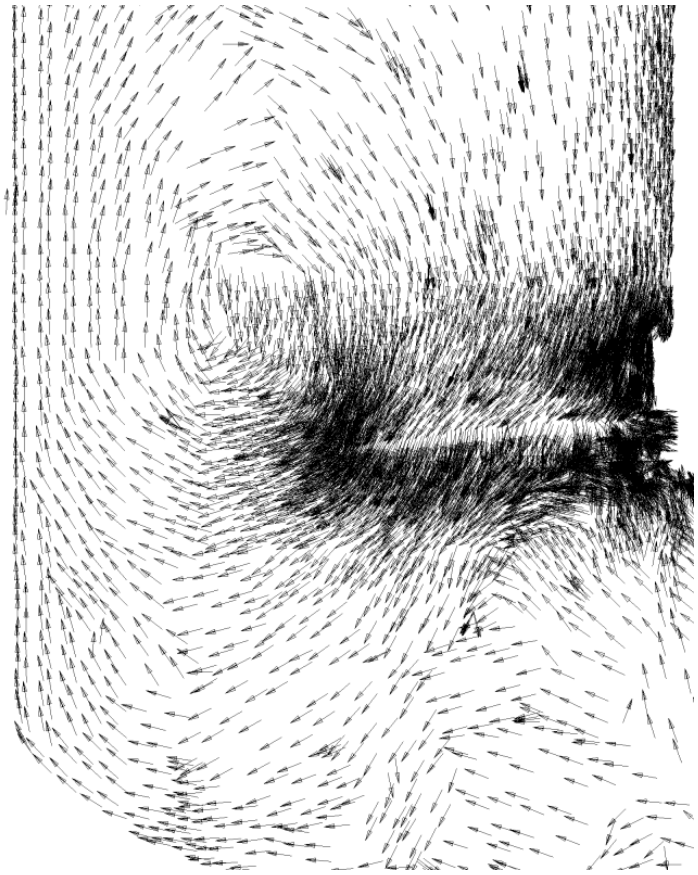

Figure 17: Vector plot at C/T=0.40

However, when the *C/T* ratio was increased starting from 0.15 to 0.40 the axial mass flowrate increased by 24.58%. This was because below *C/T* = 0.4, the spherical bottom helped to deflect the axial and radial flow toward the baffles which then directed the flow upwards, as shown in Figure 17. The upward flow at some point re-entered the impeller from the top before emerging from the blade

tips. Thus, increasing the amount of fluid moving upwards, through the use of a spherical bottom, will help to discharge higher downward axial flow.

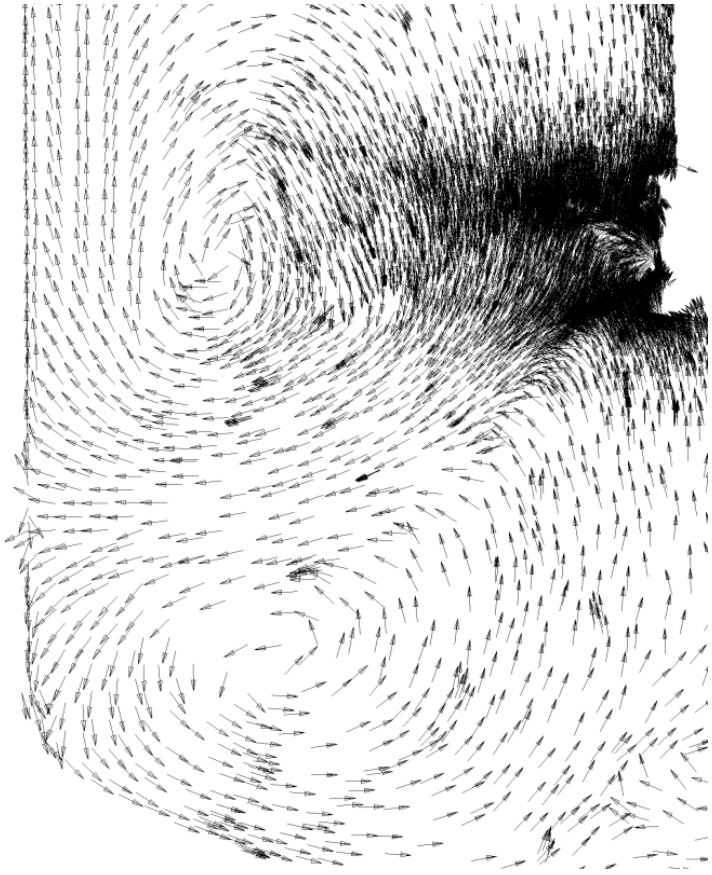

Figure 18: Vector plot at C/T=0.50

Beyond *C/T* = 0.4, increasing the *C/T* ratio will cause a decrease in the mass flowrate. Starting from *C/T* = 0.5, a significant component of the flow discharged from the impeller was travelling downwards along the wall baffle. This downward flow was then directed by the spherical bottom before joining the impeller from the bottom side, as shown in Figures 18 and 19. This negated the axial flow discharged moving in a downward direction, thus reducing the net axial mass flowrate. This occurred because beyond this maximum value, a major component of the flow discharged came into contact with the baffles first and before being deflected downwards.

Hence, the ideal situation should consist of having the flow discharge coming into contact with the spherical bottom first before being deflected

DOI: 10.2202/1934-2659.1334

upwards by the baffles. From here it can be seen that for optimal performance, $0.15 \leq C/T \leq 0.4$.

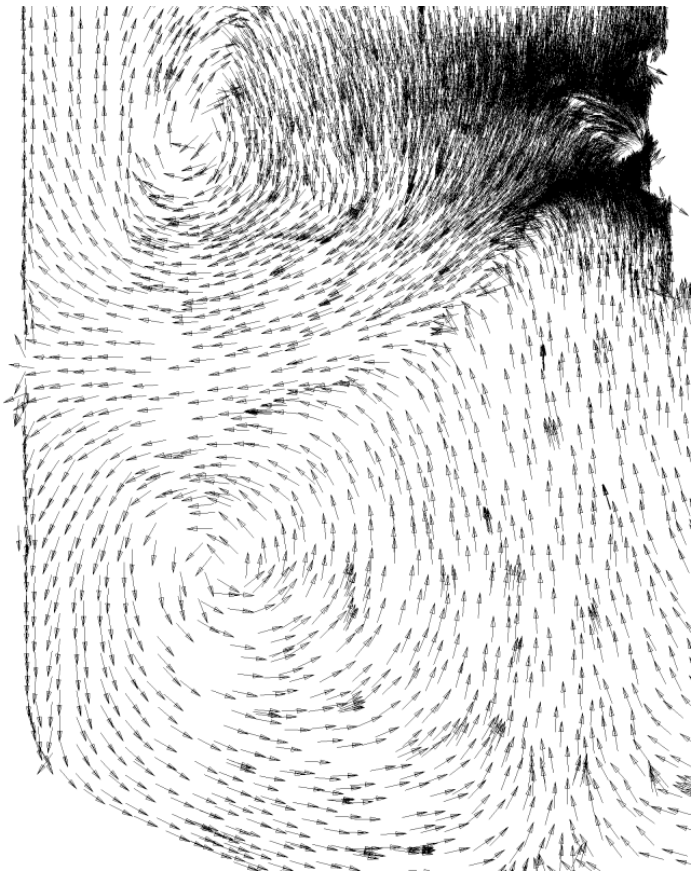

Figure 19: Vector plot at C/T=0.60

The power consumed in kilowatts as a function of impeller clearance can be represented by a third-order polynomial expression with a good regression of 0.9854, as shown in Figure 20. It can be expressed as:

$$P = -53039\left(\frac{C}{T}\right)^3 + 84461\left(\frac{C}{T}\right)^2 - 41244\left(\frac{C}{T}\right) + 11641 \qquad \text{- 13}$$

Minimum power consumption can be obtained at $C/T = 0.38$

Increasing the C/T ratio from 0.15 to 0.3 reduced the power consumption rate by 24.23%. Increasing the C/T ratio from 0.4 to 0.6 will cause an 11.04% increment in the power consumed. The reduction in power consumption was due to the lack

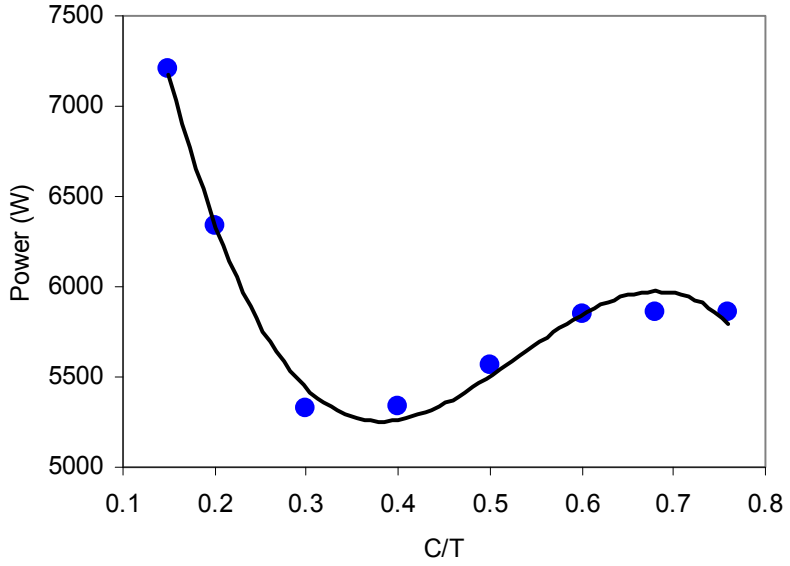

Figure 20: Power consumed in kilowatts vs C/T

of interference as the impeller was moved further away from the tank bottom. Beyond the minimum point, the power consumption increased again due to the change in the flow pattern where resistance from the baffles was significant.

5.6 Impeller rotational speed, rpm

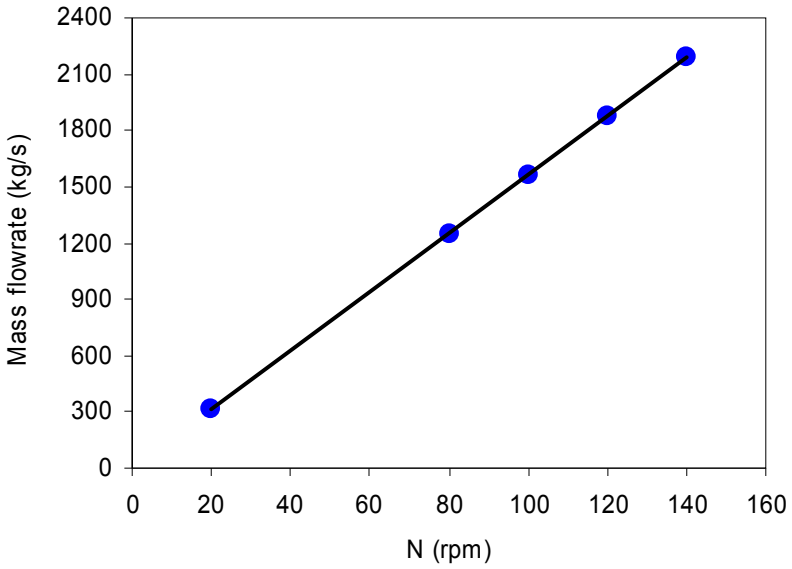

Figure 21: Mass flowrate vs impeller rotational speed

DOI: 10.2202/1934-2659.1334

Figure 21 shows that the mass flowrate increased when the impeller rotational speed was increased. This follows a linear relationship, with regression of 1 and can be expressed in the form:

$$\dot{m} = 15.65N \qquad \text{- 14}$$

An increase in the speed by 1% results in 1% increase in the axial mass flowrate. The recommended impeller rotational speed is any speed that is much greater than the just suspended speed, N_{js}.

The Zwietering [1958] correlation for determining the minimum rotational speed required to lift the particles from the tank bottom and that no particles remain on the tank bottom for any longer than 1-2 seconds is given by:

$$N_{js} = S\nu^{0.1}\left[\frac{g(\rho_s - \rho_l}{\rho_l}\right]^{0.45} X^{0.13} d_p^{0.2} D^{-0.85} \qquad \text{- 15}$$

where

S	= Zwietering constant	-
ν	= kinematic viscosity	$m^2\ s^{-1}$
g	= gravitational constant	$m\ s^{-2}$
ρ_s	= density of solid media	$kg\ m^{-3}$
ρ_l	= density of liquid media	$kg\ m^{-3}$
X	= solid loading	-
d_p	= diameter of solid particles	m
D	= impeller diameter	m

Figure 22 shows the power consumed as a function of the impeller rotational speed. The power function with a regression of 1, can be expressed as:

$$P = 0.0103(N)^{3.0222} \qquad \text{- 16}$$

Increasing the speed by 300% from 20 rpm to 80 rpm will increase the power consumption by 5,812%, that is, a 1% increase in the speed in this range will increase the power consumption by 19.37%. Increasing the speed from 80 rpm to 140 rpm (75%) will increase the power consumption by 442.7%. Therefore for every percent increase in the speed, the power consumed will increase by 5.902%.

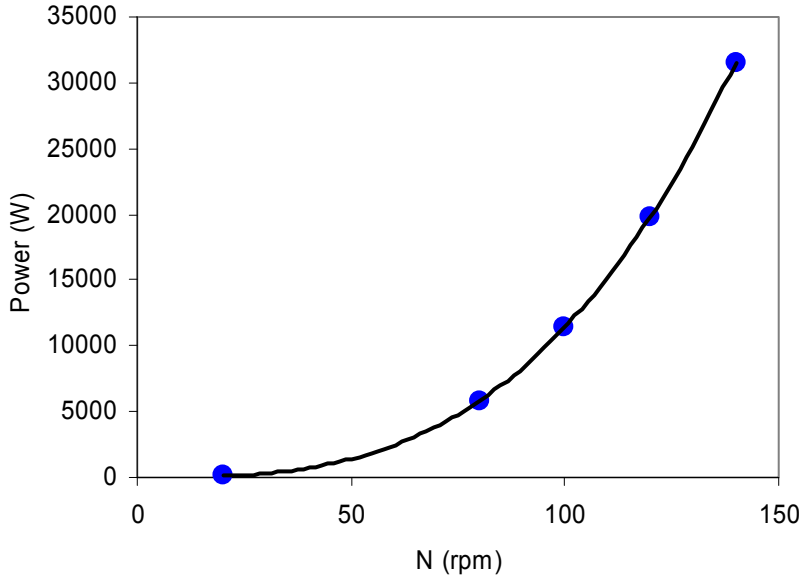

Figure 22: Power consumed in kilowatts vs N in revolution per minute

5.7 Baffle width to tank diameter ratio

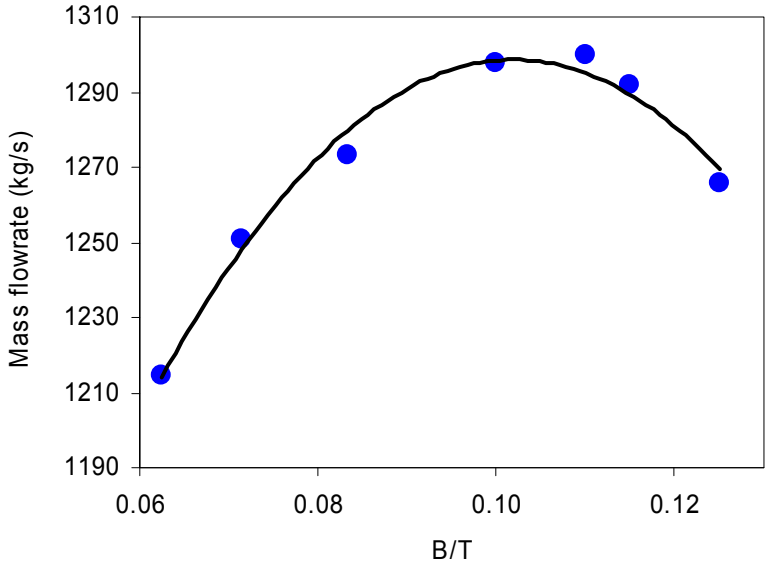

Figure 23: Mass flowrate vs B/T

DOI: 10.2202/1934-2659.1334

Figure 23 shows the relationship between the mass flowrate and the impeller diameter to tank diameter ratio. Its behaviour is governed by a quadratic expression, having a good regression of 0.9823. The mathematical expression is given by:

$$\dot{m} = -54270\left(\frac{B}{T}\right)^2 + 11064\left(\frac{B}{T}\right) + 734.7 \qquad - 17$$

For optimum performance, $B/T = 0.1019$

The purpose of baffles is to convert radial flow into axial flow. The maximum value is at $B/T = 0.1019$, which explains why most baffles in the industry have widths ranging from 1/12 to 1/10 because beyond 1/10, the mass flowrate started to drop. When the baffle widths were too small, the flow resistance was small which means the amount of radial flow converted to axial flow was minimal.

An increase in the conversion can be achieved by widening the baffle width since doing so will increase the amount of flow resistance. But as baffle width was further widened, too much flow resistance was provided by the baffles to such an extent that not much radial flow was available to be converted to axial flow. As a consequence beyond $B/T = 0.1019$, the mass flowrate started to drop. From here it can be seen that for standard wall baffles, the optimum B/T ratio is 1/10.

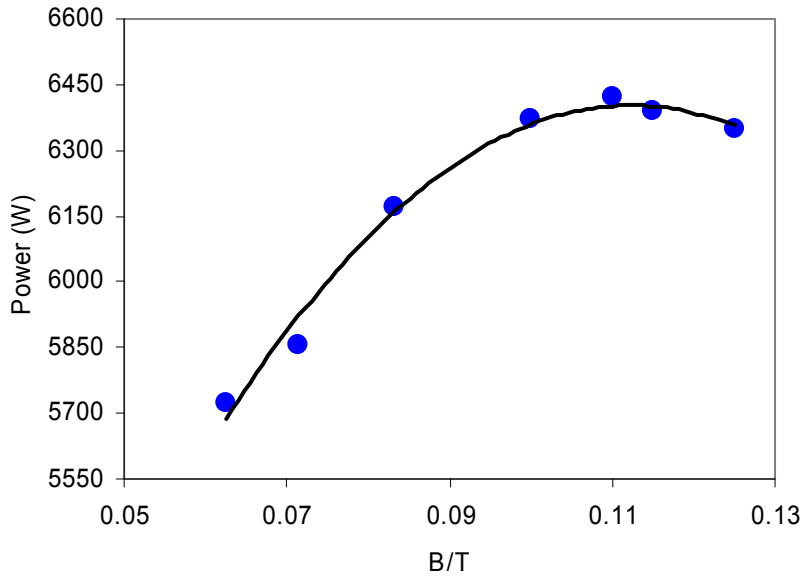

Figure 24: Power consumed in kilowatts vs B/T

As shown in Figure 24, the power consumption as a function of the baffle widths can be expressed with a good regression of 0.9872 as:

$$P = -288907\left(\frac{B}{T}\right)^2 + 64864\left(\frac{B}{T}\right) + 2762 \qquad \text{- 18}$$

Increasing *B/T* value from 0.063 to 0.10 (58.73%) will increase the power consumption by 369.6%. Increasing the *B/T* value from 0.10 to 0.15 (50%) will cause a reduction in the flowrate by 44.07%.

5.8 Baffle spacing to tank diameter ratio

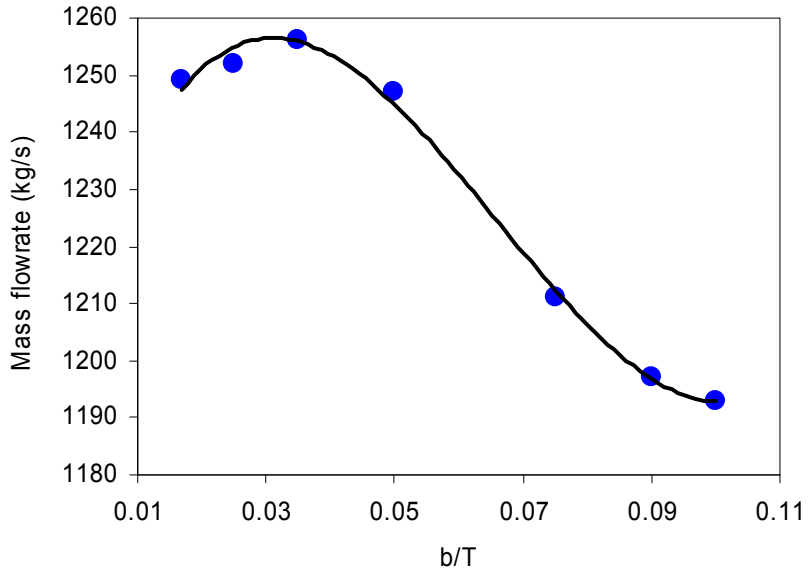

Figure 25: Mass flowrate vs b/T

Figure 25 shows the relationship between the mass flowrate and the impeller diameter to tank diameter ratio and is governed by the following third-order polynomial expression with good regression of 0.9961:

$$\dot{m} = 376766\left(\frac{b}{T}\right)^3 - 74426\left(\frac{b}{T}\right)^2 + 3529\left(\frac{b}{T}\right) + 1207 \qquad \text{- 19}$$

The maximum value is at $b/T = 0.031$

DOI: 10.2202/1934-2659.1334

From the maximum value, baffle clearance produced peak mass flowrate at 1/32 (*b/T*=0.031). At small *b/T* value, the baffles were located rather far away from the impellers therefore, not much flow resistance was contributed by them. This means that not much radial flow was converted to axial flow. As the clearance widened, the baffles were closer to the impellers thereby converting most of the radial flow to axial flow. This automatically maximised the mass flowrate traversing in the axial direction. However, as the clearance was further widened, the flow resistance dropped because the clearance was large enough for the fluid to flow pass behind the baffles with minimal interruption. This means that placing the baffles too far away from the tank wall will cause a reduction in the axial flowrate because the baffles do not convert enough radially oriented flow to axially oriented flow.

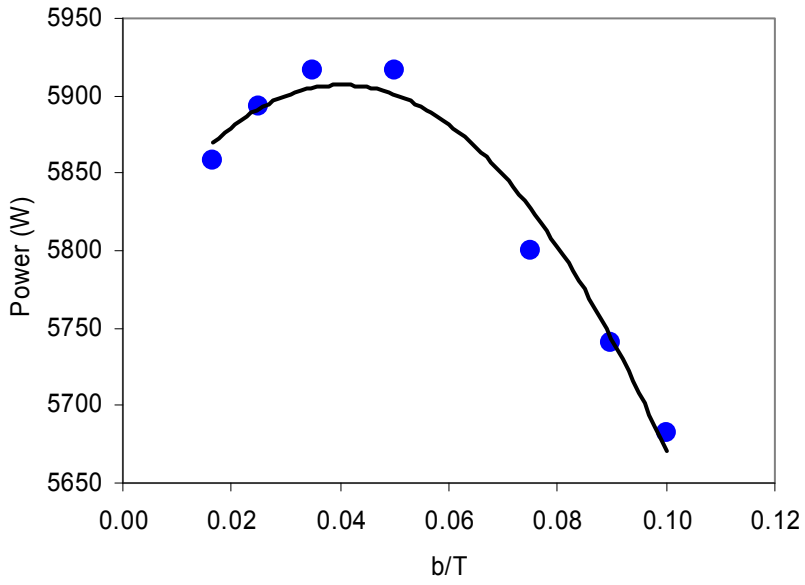

Figure 26: Power consumed in kilowatts vs b/T

The power consumption as a function of various values of *b/T*, shown in Figure 26, can be expressed by a quadratic expression with a good regression of 0.9715 as:

$$P = -66405\left(\frac{b}{T}\right)^2 + 5356\left(\frac{b}{T}\right) + 5799 \qquad \text{- 20}$$

The peak power consumption occurred at $b/T = 0.04033$

The power increased from 1/60 to 1/30 but beyond this *b/T* value, the power consumption started to decrease. At small *b/T* value, the baffles were located rather far away from the impellers therefore, little flow resistance was created. As the spacing widened, the baffles were closer to the impellers therefore contributing more flow resistance. However, as the spacing was further widened, the flow resistance dropped because the spacing was large enough for the fluid to flow behind the baffles with minimal interruption. This phenomenon caused a reduction in the power consumption.

5.9 Number of baffles

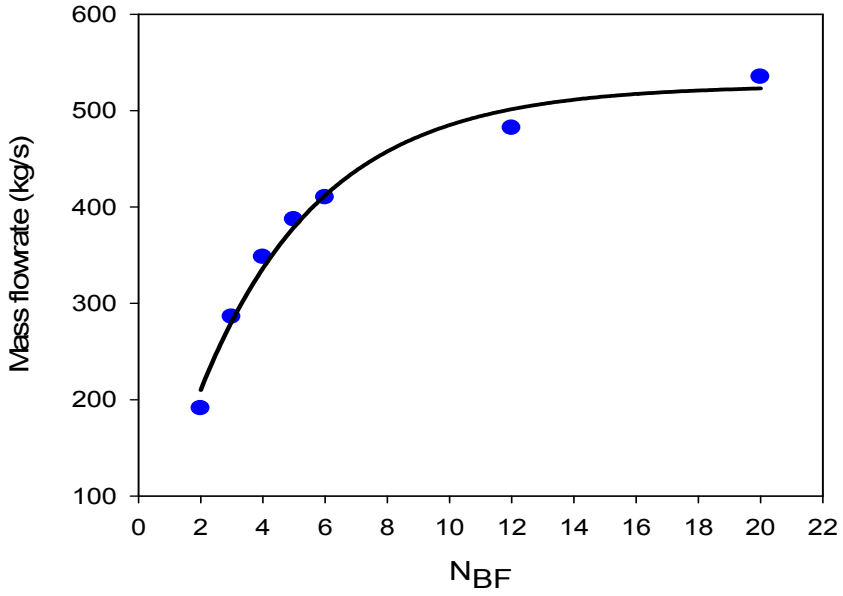

Figure 27: Mass flowrate vs N_{BF}

Figure 27 shows the relationship between the mass flowrate and number of baffles, which is governed by the following expression shown in Equation (21).

$$\dot{m} = \dot{m}_0 + a\left(1 - e^{-b(N_{BF})}\right) \qquad \text{- 21}$$

where $\dot{m}$ represents mass flowrate and $\dot{m}_0$ =903 kg s^{-1} and is the mass flowrate when there are no baffles employed, and N_{BF} represents the number of blades. A

DOI: 10.2202/1934-2659.1334

non-linear regression performed on Equation (21) yielded a=526.3 kg s^{-1} and b=0.2546 with an excellent correlation fit of 0.9931. Increasing the number of baffles from 2-3, 3-4, 4-5 and 5-6 resulted in an increase in axial flowrate by 6.379%, 4.645%, 3.471% and 2.574% respectively. In addition, increasing the number of baffles beyond 30 baffles did not result in any increase in the mass flowrate.

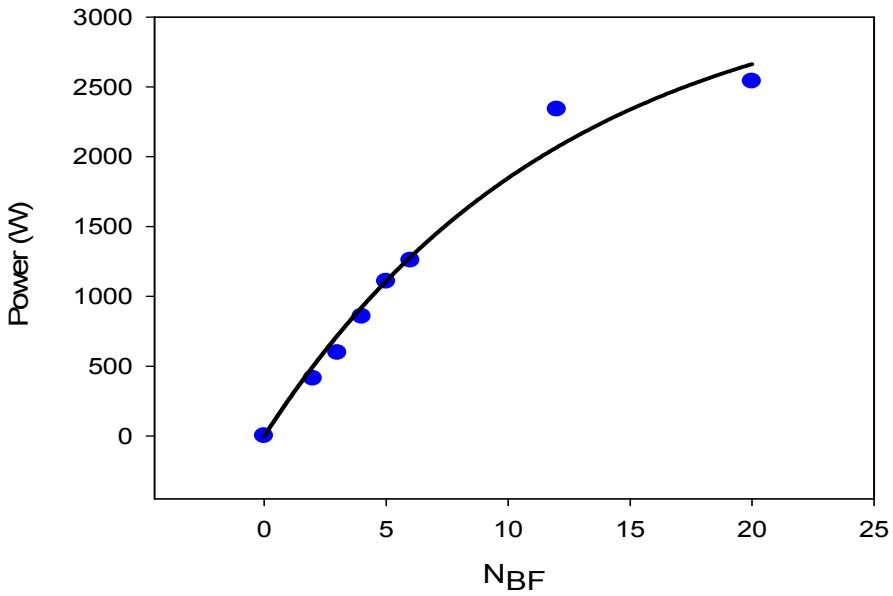

Figure 28: Power consumed in kilowatts vs N_{BF}

The power consumed as a function of the number of baffles, shown in Figure 28, can be represented by the correlation with good regression of 0.9895, in the form:

$$P = P_0 + a\left(1 - e^{-b(N_{BF})}\right) \qquad \text{- 22}$$

P is the power consumed in W, whereas P_0=5,003 W and is the power consumed when there are no baffles installed. A non-linear regression analysis on Equation (22) yielded a=3,310 W, b=0.0817. This shows that if the number of baffles is increased from 30-35, the power consumption will increase by 1.020% although no increase in mass flowrate will be attained.

5.10 Number of impellers

A simulation was conducted to determine the effect of the number of impellers on the axial mass flowrate. Five geometrical models each having a different number of impellers were created for this purpose, as shown in Figure 29. Figure 30 shows the relationship between the axial mass flowrate and the number of

Figure 29: Five mixing tanks each showing a different number of impellers

installed on the same shaft. A good correlation fit of 0.9991 was obtained for this expression. The relationship can be expressed as:

$$\dot{m} = 1250\, N_I^{0.0524} \qquad \text{- 23}$$

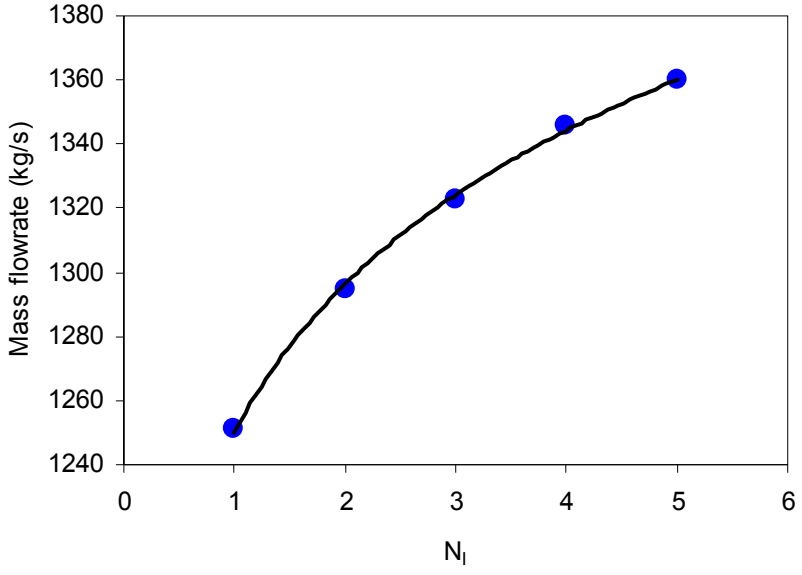

Figure 30: Mass flowrate vs number of impellers

DOI: 10.2202/1934-2659.1334

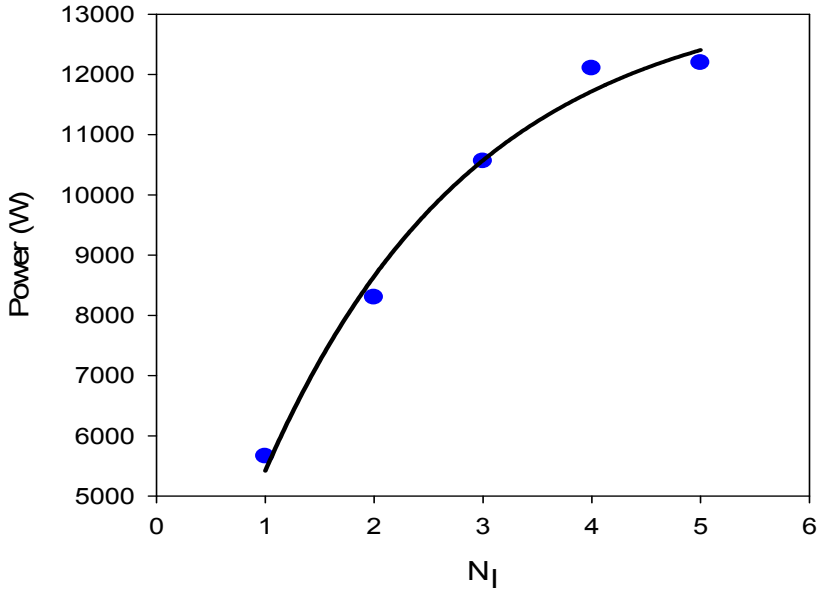

Figure 31: Power consumed in kilowatts vs number of impeller

Figure 31 shows the relationship between the power consumed by the process and the number of impellers installed on the same shaft. It can be represented by the following correlation having an excellent regression of 0.9940:

$$P = P_0 + a\left(1 - e^{-b(N_I)}\right) \qquad \text{- 24}$$

P is the power consumed in W, whereas P_0=200 W and is the power consumed when there is no impeller installed. A non-linear regression analysis on Equation (24) yielded a=13,417 W, b=0.5172. The percentage increment in the power consumed as a function of the increment in the number of impellers is best represented by the bar chart as shown in Figure 32.

For $Z/T \leq 1.4$, $N_I = 2$ since beyond this number, the increase in the flowrate did not warrant the increase in the power consumption.

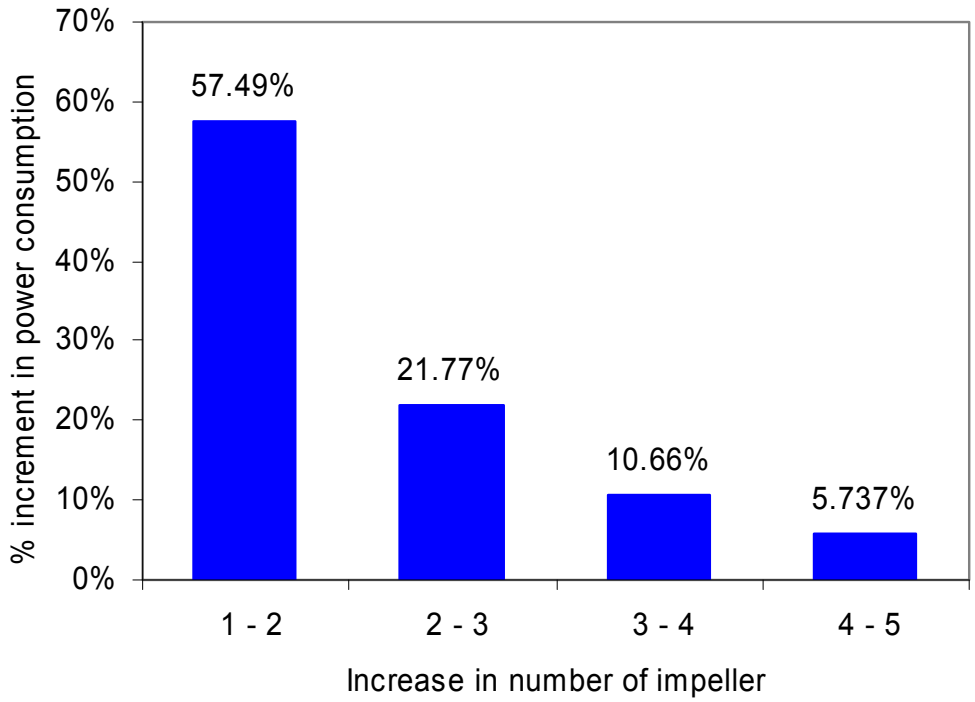

Figure 32: Percentage increment in power consumption vs increase in number of impellers

6. APPLICATION RANGE

To establish that the results presented in previous sections are also applicable to different speeds, the trials were repeated at speeds ranging from 120 rpm to 200 rpm.

Figures 33-36 each represents a plot of the mass flowrate versus a crucial variable. In each plot, the four curves represent impeller speed at 80 rpm (blue circles), 120 rpm, 160 rpm and 200 rpm, starting from the bottom most curve moving upwards as the impeller speed increased. From these studies, it can be concluded that the results discussed previously on these four variables are valid from 80 to 200 rpm.

Similarly, Figures 37-40 each represents a plot of the mass flowrate versus a crucial variable. In each plot, the four curves represent impeller speed at 80 rpm (blue circles), 120 rpm, 160 rpm and 200 rpm, starting from the bottom most curve moving upwards as the impeller speed increased. From these studies, it can be concluded that the results discussed previously on these four variables are valid from 80 to 200 rpm.

DOI: 10.2202/1934-2659.1334

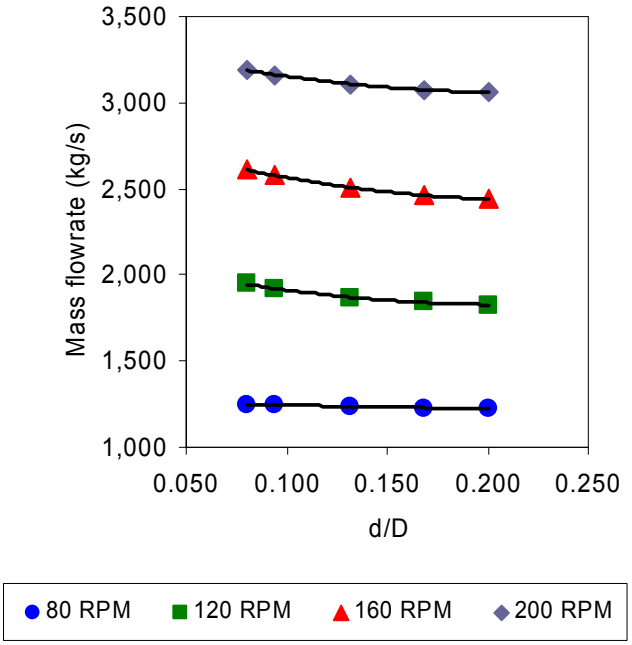

Figure 33: Mass flowrate vs d/D

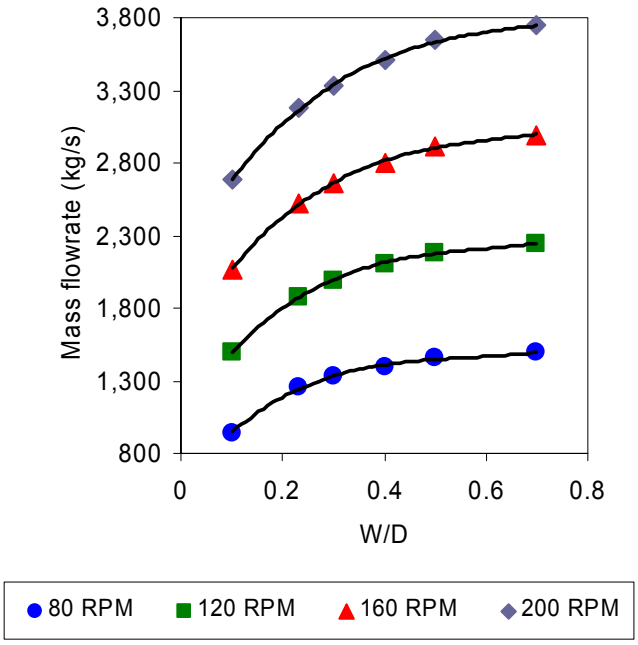

Figure 34: Mass flowrate vs W/D

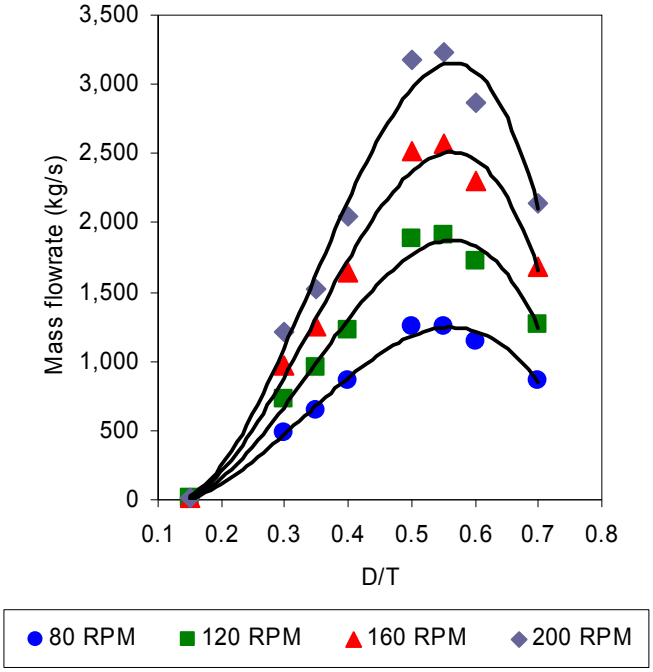

Figure 35: Mass flowrate vs D/T

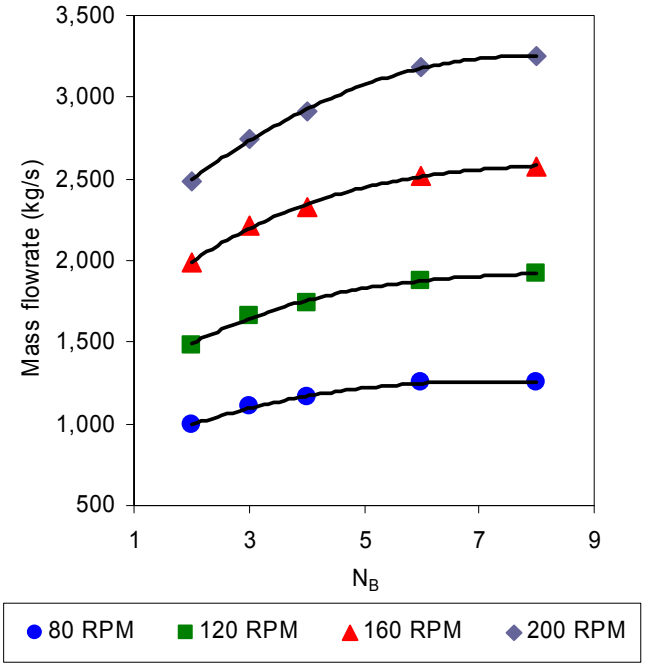

Figure 36: Mass flowrate vs N_B

DOI: 10.2202/1934-2659.1334

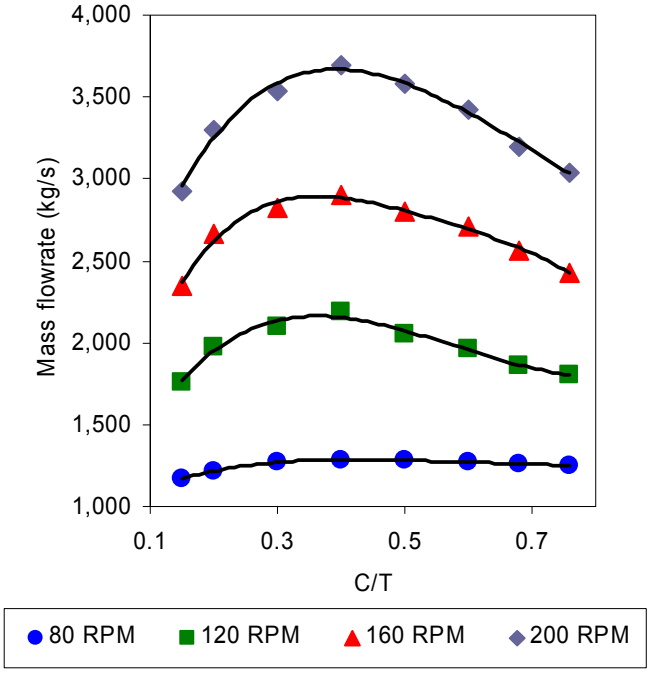

Figure 37: Mass flowrate vs C/T

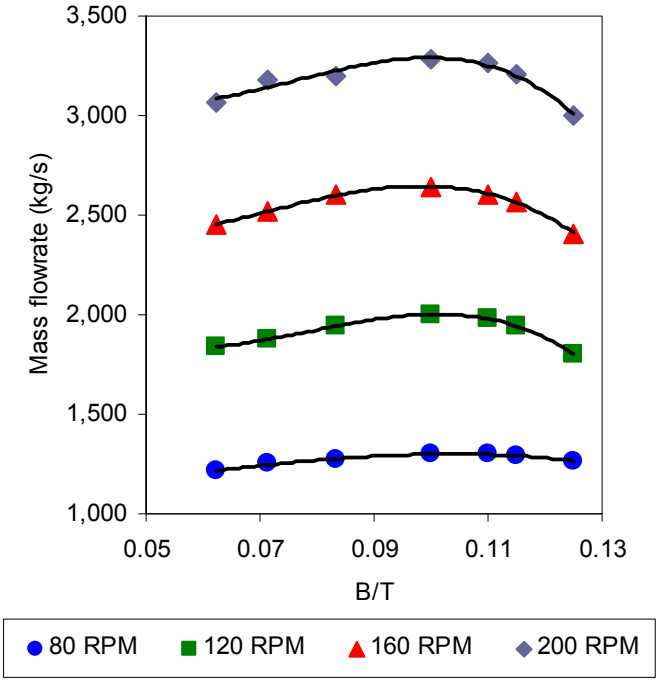

Figure 38: Mass flowrate vs B/T

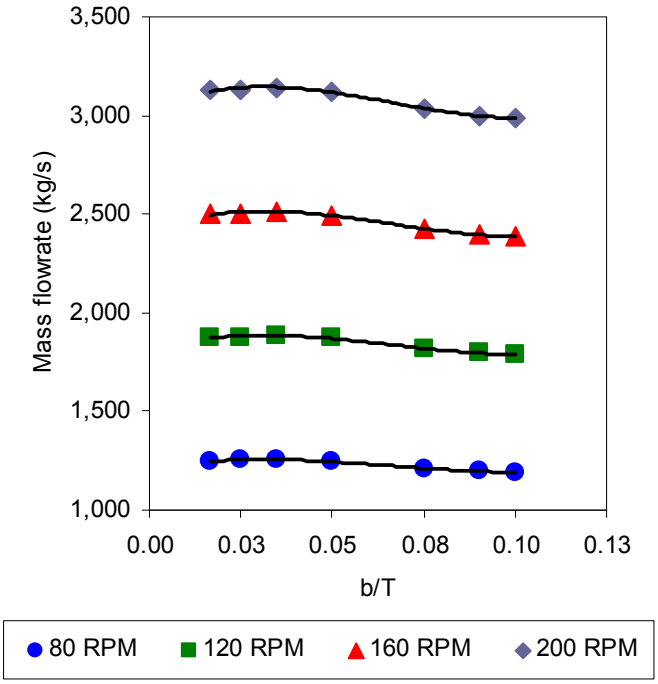

Figure 39: Mass flowrate vs b/T

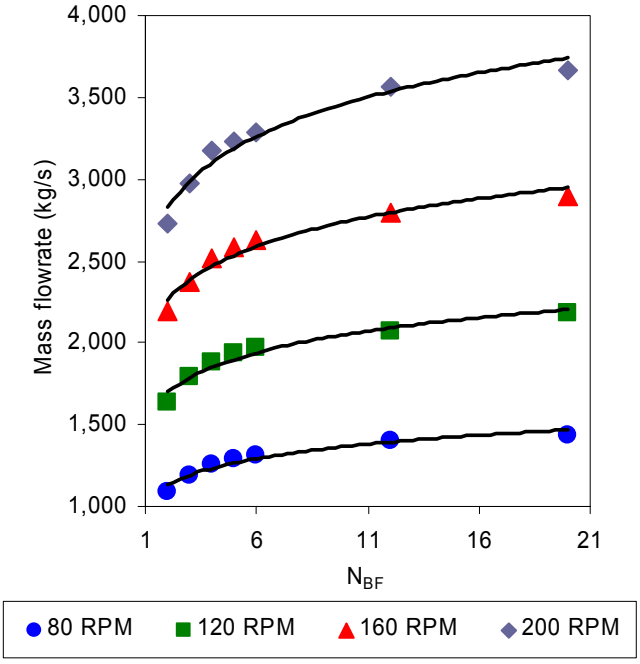

Figure 40: Mass flowrate vs N_{BF}

DOI: 10.2202/1934-2659.1334

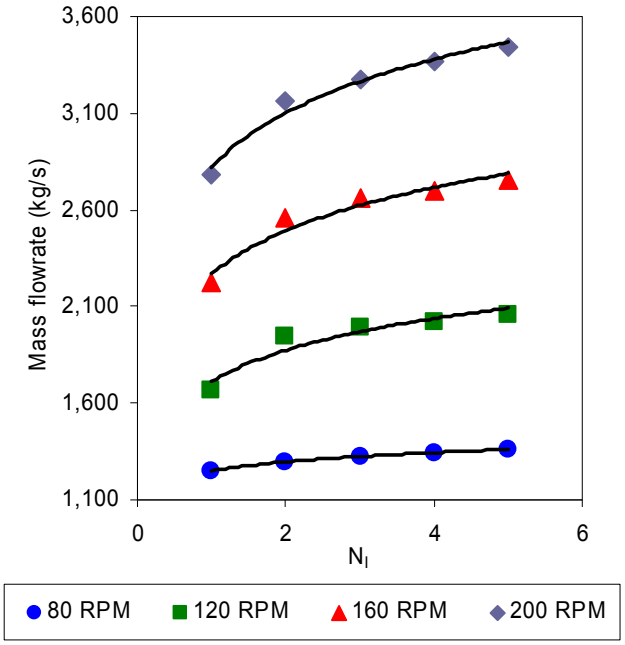

Figure 41: Mass flowrate vs N_I

Unlike the eight variables discussed previously, Figure 41 shows that the curve representing impeller speed at 80 rpm (blue circles) is almost linear whereas the curve representing impeller speeds at 120 rpm, 160 rpm and 200 rpm assume a polynomial expression. Thus, for a tank with an aspect ratio of about 1 and impeller speed ≥ 120 rpm, having more than two impellers are not recommended. This is because any system that employs more than two impellers will consume more power but deliver a marginal increase in the axial mass flowrate. Hence, the resultant benefit per unit power is insignificant when there are more than two impellers employed on the same shaft.

7. DESIGN HEURISTIC

Figure 42 presents the proposed values recommended for optimum suspension mixing performance in the form of a design heuristic. By being aware of such maximum and minimum values, engineers can avoid pitfalls and concurrently optimise the mixing tank performance to produce a more homogeneous suspension or, in the case of multiphase reactors involving solid-liquid phases, to increase the global mass transfer rate.

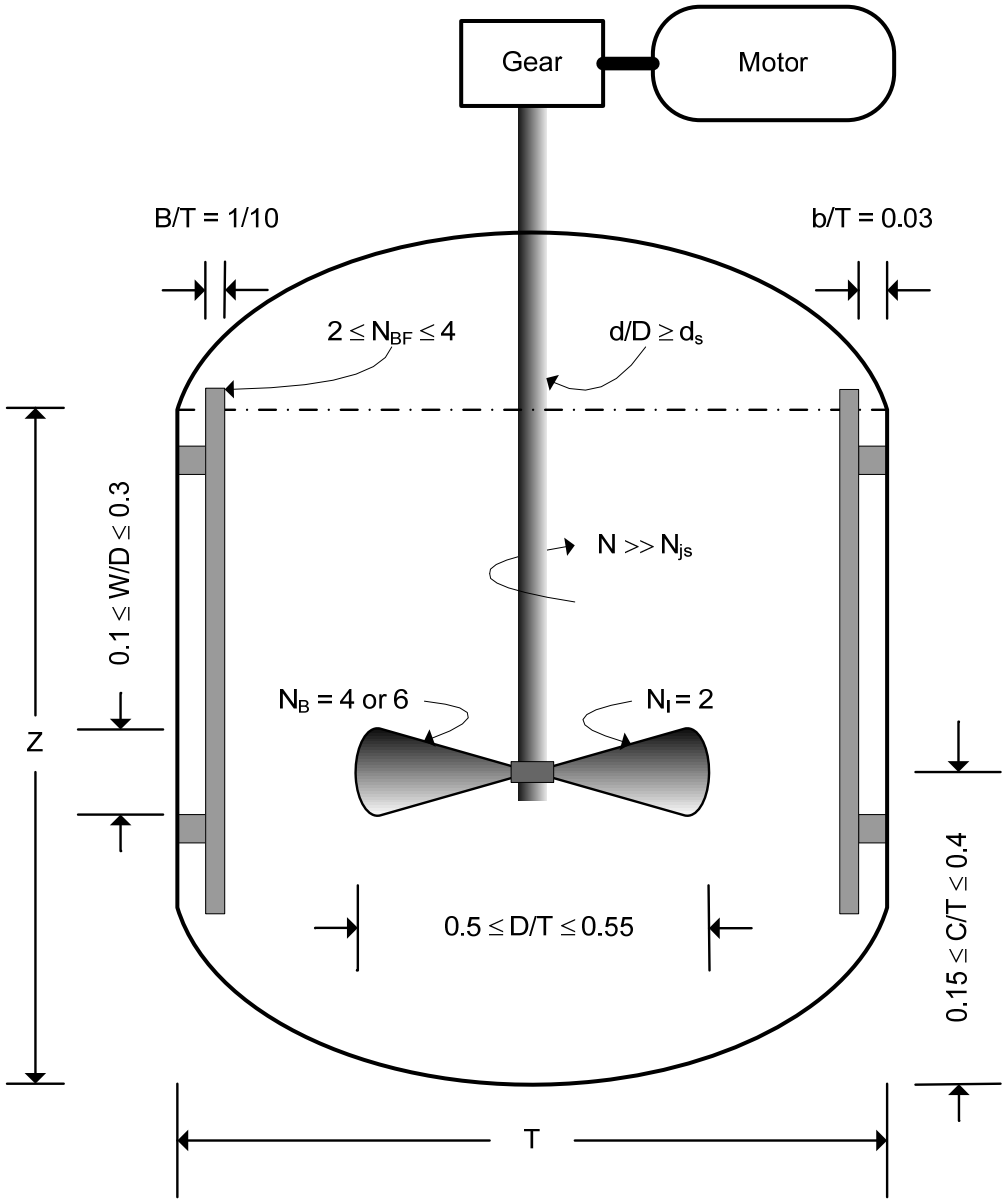

Figure 42: Summary of values for optimum suspension mixing performance

DOI: 10.2202/1934-2659.1334

8. RESULTS AND DISCUSSIONS - MULTIVARIABLE ANALYSIS

The objective of this section is to determine which two variables out of the ten variables investigated have a significant impact on the performance of a suspension mixing tank. This is achievable by conducting factorial experiments since the one-factor-at-a-time experiment is not suitable for this purpose. A full-factorial experiment involving 10 factors carried out at 5 levels requires 9,765,625 trials. Because of the economically prohibitive nature of full-factorial experiment, the partial-factorial experiment was adopted instead. Qualitek-4 software that employs the design of experiment (DOE) by Taguchi technique and this was used to create the trial condition as shown in Table 2. This technique is able to reduce a full factorial experiment to a partial factorial experiment whilst ensuring each trial condition is given a fair exposure. From the trial conditions shown in Table 2, the two most important variables are:

1. Diameter of impeller to diameter of tank ratio (*D/T*)
2. Impeller rotational speed (*N*)

The power requirement to operate the impellers in the turbulence regime is given by:

$$N_P = \frac{P}{\rho N^3 D^5} \qquad - 25$$

N_P : power number (dimensionless)
D : diameter of impeller (m)
ρ : density of fluid (kg m^{-3})
N : impeller rotational speed (rev s^{-1})

From Equation (25) and taking into consideration $P \alpha N^3$ and $P \alpha D^5$, increasing D from 0.2 to 0.5 will increase the power by $(2.5)^3 = 97.66$ times. In contrast, increasing N from 1 rev s^{-1} to 6.54 rev s^{-1} will increase the power consumption by $(6.54)^3 = 280$ times. According to Tatterson [1994], the above changes resulted in the same reduction in mixing times. In brief, increasing the *D/T* ratio is more energy efficient at reducing mixing times than increasing the value of *N*. Thus, where practical, changes to *D/T* must be given first priority over impeller rotational speed.

Table 2. Multivariable analysis trial conditions

Trials	*d/D*	*W/D*	*D/T*	N_B	*C/T*	*N*	*B/T*	*b/T*	N_{BF}
1	0.08	0.20	0.25	2	0.20	20	0.080	0.020	2
2	0.08	0.25	0.35	3	0.30	80	0.100	0.025	3
3	0.08	0.30	0.45	4	0.40	120	0.110	0.030	5
4	0.08	0.35	0.55	6	0.50	140	0.115	0.035	6
5	0.09	0.20	0.25	3	0.30	120	0.110	0.035	6
6	0.09	0.25	0.35	2	0.20	140	0.115	0.030	5
7	0.09	0.30	0.45	6	0.50	20	0.080	0.025	3
8	0.09	0.35	0.55	4	0.40	80	0.10	0.020	2
9	0.10	0.20	0.35	4	0.50	20	0.10	0.030	6
10	0.10	0.25	0.25	6	0.40	80	0.080	0.035	5
11	0.10	0.30	0.55	2	0.30	120	0.115	0.020	3
12	0.10	0.35	0.45	3	0.20	140	0.110	0.025	2
13	0.11	0.20	0.35	6	0.40	120	0.115	0.025	2
14	0.11	0.25	0.25	4	0.50	140	0.110	0.020	3
15	0.11	0.30	0.55	3	0.20	20	0.10	0.035	5
16	0.11	0.35	0.45	2	0.30	80	0.080	0.030	6
17	0.08	0.20	0.55	2	0.50	80	0.110	0.025	5
18	0.08	0.25	0.45	3	0.40	20	0.115	0.020	6
19	0.08	0.30	0.35	4	0.30	140	0.080	0.035	2
20	0.08	0.35	0.25	6	0.20	120	0.10	0.030	3
21	0.09	0.20	0.55	3	0.40	140	0.08	0.030	3
22	0.09	0.25	0.45	2	0.50	120	0.10	0.035	2
23	0.09	0.30	0.35	6	0.20	80	0.110	0.020	6
24	0.09	0.35	0.25	4	0.30	20	0.115	0.025	5
25	0.10	0.20	0.45	4	0.20	80	0.115	0.035	3
26	0.10	0.25	0.55	6	0.30	20	0.110	0.030	2
27	0.10	0.30	0.25	2	0.40	140	0.10	0.025	6
28	0.10	0.35	0.35	3	0.50	120	0.080	0.020	5
29	0.11	0.20	0.45	6	0.30	140	0.10	0.020	5
30	0.11	0.25	0.55	4	0.20	120	0.080	0.025	6
31	0.11	0.30	0.25	3	0.50	80	0.115	0.030	2
32	0.11	0.35	0.35	2	0.40	20	0.110	0.035	3

9. CONCLUSIONS

Suspension of particles via mechanical agitation in the process industry is a common goal. This paper has investigated the influence of ten industrially-recognised important variables in the design of suspension mixing tanks using a CFD model of a commercial tank. The performance of the suspension mixing tank as a function of these crucial variables was discussed in detail. For the mass flowrate investigation, out of the ten variables investigated, nine followed a non-linear relationship and one followed a linear relationship. Similarly, for the power consumed as a function of the variables, nine followed a non-linear relationship and the remaining variable obeyed a linear correlation. The derived relationships were used to optimise the tank design with respect to the variables.

A design heuristic incorporating the optimum operating range to suspend particles was developed as a result of this study. It is applicable for impeller speed rotating between 80 to 200 rpm. This practical design heuristic can be applied across a broad range of industries such as the chemical, biochemical,

DOI: 10.2202/1934-2659.1334

pharmaceutical, petrochemical, explosives and mineral processing industries. This design heuristic can be used to fill research gap and provide engineers with a platform to design an effective suspension mixing tank or to optimise and existing tanks.

Finally, from the multivariable analysis, the two most important variables that affected the performance of mixing tank in suspending particles were determined as the diameter of impeller to diameter of tank ratio (*D/T*) and the impeller rotational speed (*N*). Even so, changing the *D/T* must be given priority over *N*.

Nomenclature

$\dot{m}$: mass flowrate across plane
μ : absolute viscosity
ρ : density of fluid
ε : epsilon
ν : kinematic viscosity
υ : velocity
σ_ε : turbulent Prandtl number for ε
σ_k : turbulent Prandtl number for k
b : baffle spacing
b/T : baffle spacing to tank diameter ratio
B/T : baffle width to tank diameter ratio
C/T : impeller bottom clearance
$C_{1\varepsilon}$: constant
C_2 : constant
D : diameter of impeller
d/D : shaft diameter to impeller diameter ratio
D/T : impeller diameter to tank diameter ratio
d_p : diameter of solid particles
g : gravitational constant
G_b : turbulence kinetic energy due to buoyancy
G_k : turbulence kinetic energy generated due to the mean velocity gradients
k : kinetic energy
KPI : key performance indicator
MRF : multiple reference frame
N : impeller rotational speed

N_B : number of blades in the impeller
N_{BF} : number of baffles
N_I : number of impellers
N_{js} : just suspended speed
N_P : power number
P : power consumed
P : pressure
PIV : particle image velocimetry
RDX : research department explosives
S : Zwietering constant
SIMPLE: semi-implicit method for pressure linked equations
T : tank diameter
t : time
VOF : volume of fluid
W/D : blade width to impeller diameter ratio
X : solid loading
Y_M : contribution of the fluctuating dilation to the overall dissipation rate

References

Alliet-Gaubert M., Sardeing R., Xuereb C., Hobbes P., Bertrand L. and Swaels P., CFD analysis of industrial multi-staged stirred vessels, Chemical Engineering and Processing (2006), Vol 45, 415-427

Aubin J. and Xuereb C., Design of multiple impeller stirred tanks for the mixing of highly viscous fluids using CFD, Chemical Engineering Science (2006), Vol 61, 2913-2920

Kilander J., Blomstrom S., Rasmuson, A., Scale-up behaviour in stirred square flocculation tanks, Chemical Engineering Science (2007), Vol 62, 1606-1618

Kresta S.M., Mao D. and Roussinova V., Batch blend time in square stirred tanks, Chemical Engineering Science (2006) Vol 61, 2823-2825

Kumaresan T. and Joshi J.B., Effect of impeller design on the flow pattern and mixing in stirred tanks, Chemical Engineering Journal (2006), Vol 115, 173-193

DOI: 10.2202/1934-2659.1334

Laakkonen M., Moilanen P., Alopaeus V., Aittamaa J. Modelling local bubble size distributions in agitated vessels, Chemical Engineering Science (2007) Vol 62, 721-740

Lea J., Gehrig A., Flavel P. and Adesina A.A, The computational fluid dynamics modelling and simulation of nitrator employed for the manufacture of military propellant, ICCHMT May 17-20 2005, Paris, France

Lewis A.E. and Ochieng A., CFD simulation of solids off-bottom suspension and cloud height, Hydrometallurgy (2006) Vol 82, 1-12

Paul E.L., Atiemo-Obeng V.A. and Kresta S.M., Handbook of industrial mixing – science and practice, Wiley Interscience (2004)

Rahimi M. and Parvareh A., Experimental and CFD investigation on mixing by a jet in a semi-industrial stirred tank, Chemical Engineering Journal (2005) Vol 115, 85-92

Sommerfeld M. and Decker S., State of the art and future trends in CFD simulation of stirred vessel hydrodynamics, Chemical Engineering Technology (2004) Vol 27, No. 3

Tatterson G.B., Scaleup and design of industrial mixing processes, McGraw-Hill Inc (1994)

Zwietering T.N., Suspending of solid particles in liquid by agitators, Chemical Engineering Science (1958) Vol 8, 244-253